University of BRISTOL

DEPARTMENT OF PHYSICS

FINAL YEAR INDUSTRIAL GROUP PROJECT

NAME:	Max Brackhaus, Max Dolan, James McDougall, Annabel McGrath
DEGREE COURSE:	Physics BSc
PROJECT TITLE:	Particle Detector for CERN's Experimental Areas
YEAR OF SUBMISSION:	2023
SUPERVISOR:	Sudarshan Paramesvaran
NUMBER OF WORDS:	8880

Declaration

We did not collect all of the data presented in this project. We did gather all data involving visible light and the Caesium-137 radioactive source, however Dr David Cussans supervised the gathering of data using the Americium-241 source. We performed all of the analysis on this data ourselves, using our own code. Dr David Cussans also helped us design the read-out electronics used for collecting data from the scintillator, but we performed the assembly ourselves. We divided the testing process of this circuit evenly between all members of the group.

Contents

Executive Summary

The European Organisation for Nuclear Research (CERN) make use of secondary beams provided by its accelerators, made up of leptons and hadrons with varying intensities, for a range of experiments within its different experimental areas. Most of the current implementation used for the measurement of the intensity of these beams is ageing and in need of renewal.

The objective of this project was to design a scintillating trigger for implementation in the North Experimental Area of CERN, to update the old technology currently in place. Specific to this application, the trigger, which creates a flash of light when a particle passes through it, aims to measure every particle that passes, giving a beam intensity measurement of the secondary beams in the North Area and also pass information on to different particle detectors in the beamline.

The design proposed in this report is comprised of four main components, namely, a plastic scintillating tile, wavelength shifting fibres, photodetectors (silicon photomultipliers) and a read-out electronics system. The scintillating tile transforms the high energy particles that collide with its surface into photons in the visible range. The wavelength shifting fibres, two placed at opposing edges of the tile, work to absorb higher frequency photons and emit them at a lower frequency which is better suited to the absorption peak of the silicon photomultiplier used. Photodetectors in general convert photons to an electrical signal suitable for data collection and analysis purposes. Silicon photomultipliers were chosen due to their reliability and wide availability.

This first prototype has been tested initially with visible light to establish that the unit was sensitive to light, and later with a radioactive source to replicate the secondary beams it is designed to measure in CERN's North Area.

LTspice simulations have been carried out to provide an estimate of the data we expected to record. These simulations were confirmed when testing began with a pulsed LED and again with the radioactive source testing.

Despite initial high levels of noise, single-pixel avalanches have been identified and the number of dark counts quantified. The specification of the beam and these dark count measurements can be used to indicate the intensity of the beam.

Acknowledgements

1 Introduction

1.1 Particle Physics and CERN

During the last century, over a quarter of the Nobel Prizes in Physics have been awarded to work directly related to developments relating to the Standard Model. This is the best theory to date of a description of the fundamental particles that make up the universe and how these interact with each other via three of the four fundamental forces: electromagnetism, the strong and weak forces [1] [2]. Notably, gravity is not included despite the theory's accurate predictions [3].These elementary particles can be split into two types of matter, quarks and leptons, and force particles, bosons, which are responsible for the four fundamental forces and giving particles mass. Figure 1 provides a summary of the different particles and their properties relevant to this investigation.

	Particle type	Rest mass [MeV/c]	Mean life τ [s]	Main decay mode
Photons	(γ)	0	Stable	–
Leptons	Electron (e$^-$), positron (e$^+$)	0.511	Stable	–
	Muon (μ^+, μ^-)	105.66	2.2×10^{-6}	$\mu^- \to e^- \bar{\nu}_e \nu_\mu$
				$\mu^+ \to e^+ \nu_e \bar{\nu}_\mu$
Hadrons	Proton (p)	938.27	Stable	–
	Neutron (n)	939.57	880	$n \to pe^- \bar{\nu}_e$
	Charged pion (π^+, π^-)	139.57	2.6×10^{-8}	$\pi^- \to \mu^- \bar{\nu}_\mu$
				$\pi^+ \to \mu^+ \nu_\mu$
	Neutral pion (π^0)	134.98	8.5×10^{-17}	$\pi^0 \to \gamma\gamma$

Figure 1: The mass, mean life, and main decay mode of the most relevant particle species found in hadron and lepton environments at CERN [7].

The road to completion of the Standard Model has not been a short journey, starting in 1897 with J.J. Thompson's discovery of the electron and ending with the discovery of the Higgs Boson in 2012 at the Large Hadron Collider at the European Council for Nuclear Research (CERN) [4] [5].

In order to discover new particles and learn more about others, particles must be given enormous amounts of energy. This is achieved by colliding two primary beams of protons at relativistic speeds. CERN, just 2 years ago (2021) found four new particles for a total of 59 new particles found [6].

Particle discoveries and other investigations in the Experimental Areas of CERN that learn more about existing components of the Standard Model, mostly make use of secondary beams [9]. These beams are composed of particles that are produced where a primary beam is brought into collision with a target, usually beryllium, at the so-called 'interaction points' of a collider, a process depicted in Figure 2 [7]. Such particles are leptons and hadrons with energies ranging from $1 GeV/c$ to $450 GeV/c$, and intensities from 102 to 107 particles $s^{-1}mm^{-2}$ [8]. The intensity of these secondary beams has been measured since the late 1970s using detectors such as Scintillator Paddles and Filament Scintillators (FISCs), which will be discussed in chapter 1.3 [9].

1.2 The North Experimental Area

The North Experimental Area (NA) is made up of the SPS, the M2 muon beam, the K12 kaon beam and the H2, H4, H6 and H8, mostly test beam lines (Figure 3(b)). This report will focus on the NA as it is in this area where the particle detector instrumentation is being replaced, with funding from the North Area Consolidated Grant (NA-CONS) [10]. The current instrumentation,
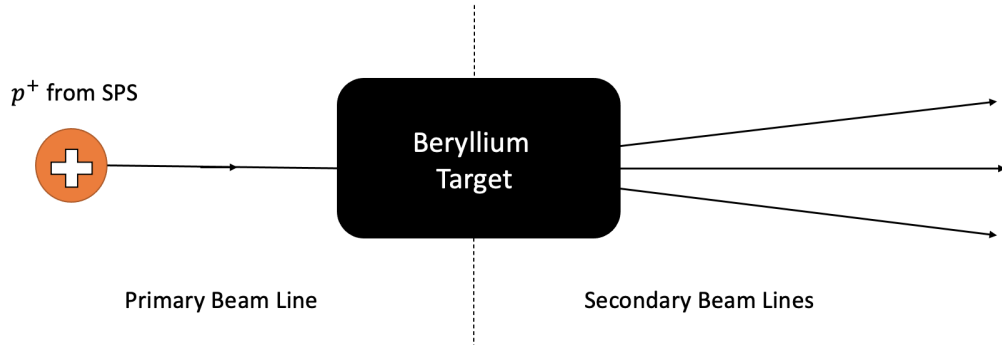
Figure 2: A very simplified schematic showing the process of secondary beam production, where protons from the Super Proton Synchotron (SPS) are brought into collision with a Beryllium target. These reactions occurs at specific locations within the accelerator called 'interaction points'.

named above, dates from when the North Area first opened in 1978, and is therefore degrading and becoming difficult to maintain, as many of the experts in this technology have now retired [9].
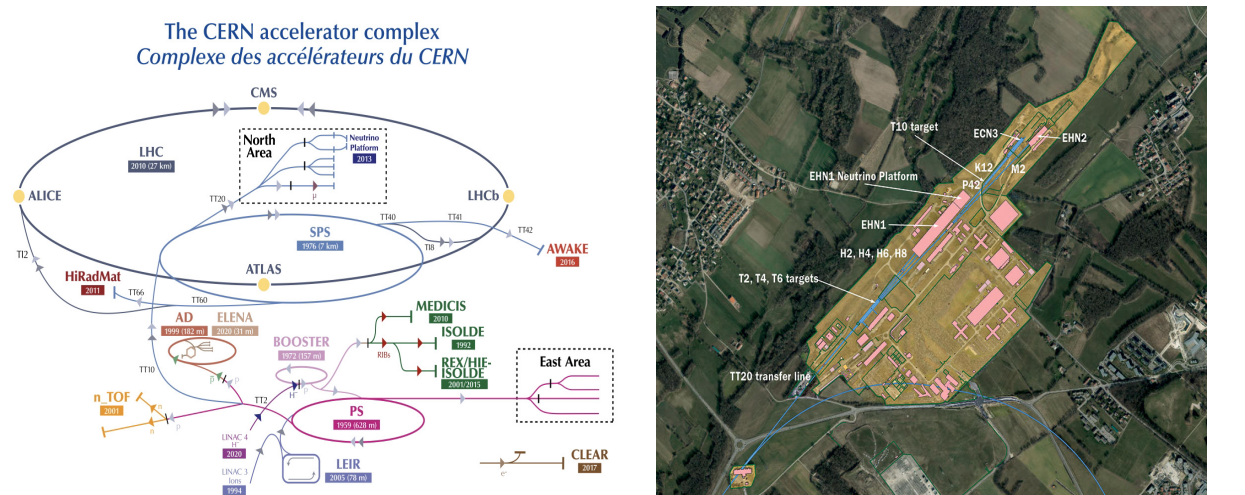
(a) Diagram of the CERN accelerator complex in January 2022

(b) Satellite image of the North Area, labelled with the main beam lines

Figure 3: Images of the facilities at CERN, showing the scale and complexity of the experimental facility [11].

1.3 Present Instrumentation

As previously mentioned, there are a few different types of intensity detector currently in use in the NA. Those briefly reviewed here are Scintillating Paddles, Filament Scintillators (FISCs), Cherenkov Threshold Counters (CETs) and Cherenkov Differential Counters with Achromatic Ring focus (CEDAR) [16].

1.3.1 Scintillating Paddles

Scintillating paddles are widely used to measure the intensity of secondary beams in the North Area. Their assembly, as shown in Figure 4, is as follows; a large plastic scintillating tile is

connected to a photomultiplier tube (PMT), via a light guide, to direct the scintillations to the photodetector. They are able to count the passage of every particle that passes and can be used to generate trigger signals for other detectors.

Figure 4: Scintillator paddle with attached PMT in the laboratory (left) and in the beam line surrounded by a purple frame (right). The white marker is the point at which the beam strikes the paddle. [9]
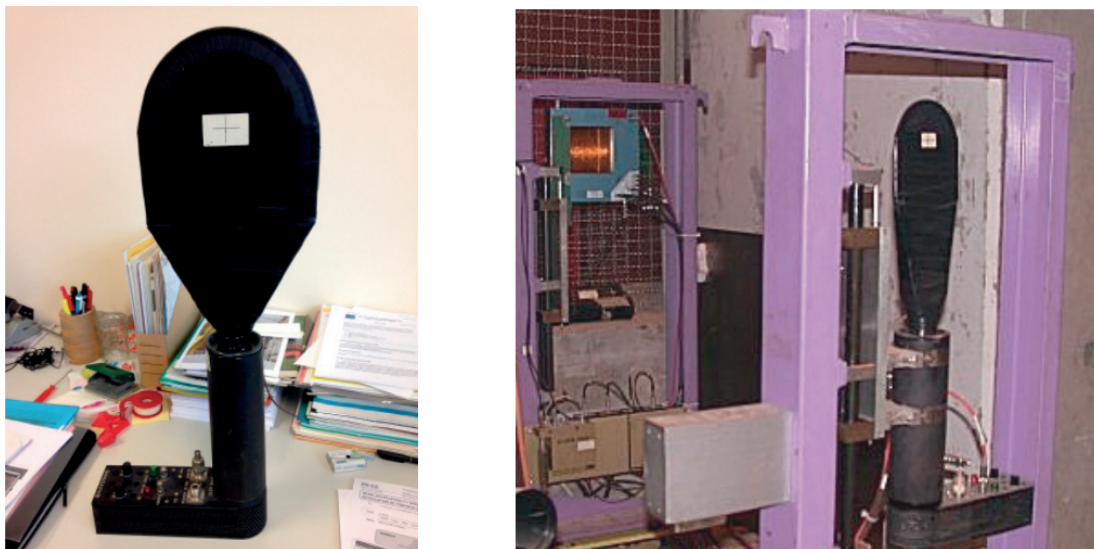
1.3.2   FISCs

FISCs are systems of thin threadlike scintillator fibres that are powered by a motor system to scan the incoming beam. In FISCs, two PMTs are used to detect the light produced from the scintillating filament. The beam is then reconfigured using signals from the PMTs and the beam's intensity can be read out. In its fast technique, a full scan is completed of one delivery of beams (spill); whereas in its slow technique, part scans are completed over multiple spills. In the North Area, typically one or two spills occur every $40.8s$. These monitors are mainly used to measure the profile of the incoming particles, and have the disadvantage that they need several minutes to produce low intensity or high resolution readings [9].

1.3.3   CETs

CETs are used for the identification of incoming particles. These detectors are large structures (several metres long) containing noble gases that can be interchanged. The light produced in the gas due to Cherenkov radiation is guided to a PMT using a mirror. This type of radiation occurs when charged particles pass through a dielectric medium at a greater speed than the phase velocity of the light in that medium [31]. The amplified signals are compared with known values for different particles above a fixed threshold and counted. Therefore these counters can count different particle types [32].

1.3.4   CEDAR Counters

Cherenkov Differential counters with Achromatic Ring focus, or CEDAR counters for short, use the same process as CETs, but have a more complex optical system which allows them to work at higher momenta [33].

(a) CET monitor
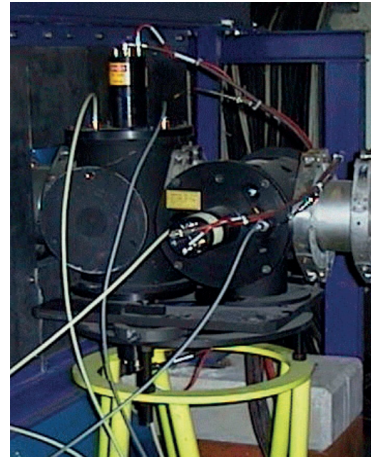
(b) FISC in beam line

Figure 5: CET monitor and FISC in the North Experimental Area [9]

Figure 6: The first CEDAR counter tested in July 1975 (Copyright:CERN) [12].

1.4 The Need for New Instrumentation

Although the aforementioned monitors still widely conduct their roles to a high standard, there are some areas in which they are failing, explaining the need for a new design. As most, if not all, of these monitors were built approximately 50 years ago, a number of issues have arisen due to their age. Firstly, the secondary beam lines emit radiation of up to $100kGy$; this has resulted in damage of the monitors, which have been withstanding this high radiation for so long. Secondly, as previously mentioned, many of the scientists and engineers (Figures 6 and 7) who are experts in this technology have now retired, resulting in a lack of expertise in repair strategies if something goes wrong. Furthermore, with funding from the NA-CONS there is currently an extension taking place for the Neutrino Platform with test beams for neutrino detector development and R&D [9]. The current size and functionality of many of these monitors therefore no longer fits the needs of the Area, specifically in dimension, functionality within a vacuum, compatibility to new profile monitors and mobility in and out of the beam line [9] [15].
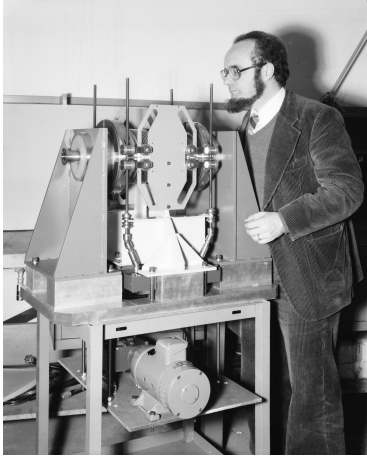
Figure 7: Scientists installing a new automatic clamp for a beam line in the North Area in 1978 (Copyright: CERN) [12].

1.5 Requirements for the Scintillating Trigger

The main objective of this project is to develop a scintillating trigger to measure the intensity of single photons passing through the scintillating material. The specific requirements for this trigger are outlined below:

- The intensity of each particle that passes through should be measured with $> 99\%$ efficiency

- The trigger should be radiation tolerant, up to approximately $100kGy$

- It must be compatitible, i.e. fully functioning, within a primary vacuum ($10^3 mbar$)

- The entire design must be easily inserted and removed from the beamline when necessary and therefore its sensitive area must not exceed a size of $10cm^2$

- The trigger must cost no more than 5000 CHF (4400 GBP (March 2023)) and should have a material budget of $X/X_0 < 0.5\%$

2 Theory

2.1 Particle Interactions with Matter

One key aspect of particle-matter interactions for this project is the energy loss of heavy, charged particles, which can be due to a range of elastic and inelastic collisions such as Coulomb scattering, nuclear scattering, Bremsstrahlung, and ionizational losses. The primary mode of energy loss for heavy, charged particles is inelastic collisions with atomic electrons [13]. This occurs due to the opposing charges of the positive incoming particles and the negative electrons, which repel according to Coulomb repulsion. Given sufficient repulsion and therefore energy transfer, the electron in the atom can either be excited up energy levels in the atom in a process called excitation or emitted from the atom entirely in ionization [17]. These are known as soft or hard collisions, respectively.
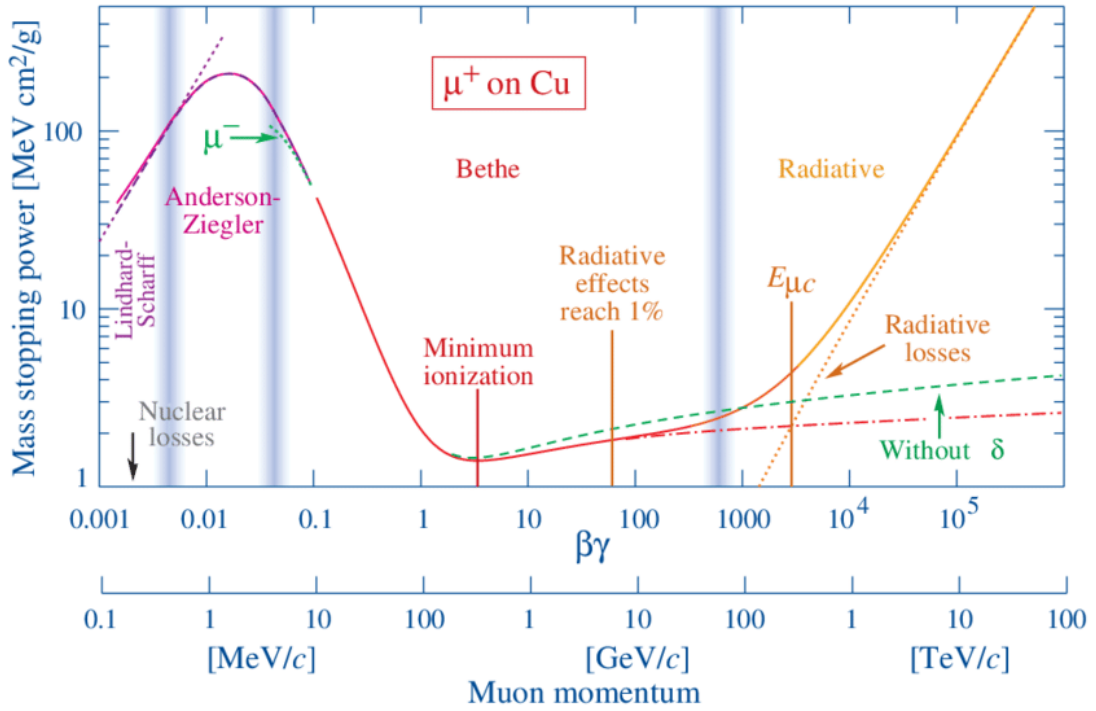
Figure 8: Mass stopping power of positively charged muons in copper. The solid line represents total stopping power, the dashed line represents radiative stopping power and the dotted, dashed line represents electronic stopping power according to Bethe. ([7]

Some electrons released from ionization have sufficient energy to cause secondary ionization in other atoms. These electrons are known as δ-rays. As the amount of energy that a charged particle can transfer to an electron in a single collision is small when compared with the total beam energy, multiple interactions take place as the charged particle passes through matter. As a result of these interactions, the velocity of the charged particle gradually decreases until it comes to a stop. In an area densely filled with electrons, such as a scintillating material, the number of collisions of heavy charged particles with electrons per unit length is high, and it is useful to define the stopping power $S(E)$ as the rate of energy loss dE per unit length dx which is given by the Bethe-Bloch equation,

$$S = -\frac{dE}{dx} = Kz^2 \frac{Z}{A\beta^2} \left(\frac{1}{2} ln \frac{2m_e c^2 \beta^2 \gamma^2 T_{max}}{I^2} - \beta^2 - \frac{\delta(\beta\gamma)}{2} \right) \tag{1}$$

11

where $K = 4\pi N_A r_e^2 m_e c^2$, z is the charge of the incident particle, Z is the atomic number of the absorbing material, A is its atomic mass, $\beta = v/c$ is the velocity of the particle as a fraction of c, the speed of light, m_e is the rest mass of an electron, $\gamma = 1/\sqrt{1 - \beta^2}$ is the Lorentz factor, and $\delta(\beta\gamma)$ is the density effect correction to the ionization energy loss [9]. This parameter S has been shown to increase as the density of the number of both the charged particles and the atoms in the incident material increases. Note that the Bethe-Bloch equation is not valid for electrons, as their small mass requires relativistic corrections, and they also incur more energy losses by Bremsstrahlung, so terms would need to be added to make it suitable. For positively charged muons, like those used in the M2 beam at CERN, their rate of energy loss in copper is shown in Figure 8. There is a local minimum here in the Bethe-Bloch equation at $\beta\gamma \approx 3 - 3.5$. Particles travelling at such velocities are commonly known as minimum ionizing particles, which refers to particles with an energy loss rate through matter that is very close to its minimum. After the proton has gone through sufficient electronic stopping, it will reach a point where it has slowed down sufficiently for the cross-sectional area, effectively probability, of the inelastic nuclear interactions to increase, at which point they become more likely to occur and end up being the main source of energy loss.

2.2 Scintillators

Scintillation is when certain molecules, excited by a charged particle traversing matter, emit a small fraction of their energ as photons in the visible range [13]. Both organic and inorganic scintillators are used in high energy physics. In the case of inorganic scintillators, the scintillation effect arises due to the crystal structure, and in organic scintillators arises from transitions in the energy level of a single molecule and therefore fluorescence is observed [9]. Due to this fluorescence, organic scintillators are faster, but they have a lower light output than the inorganic alternative. The most commonly used scintillators in particle physics are made of organic materials such as plastics, liquids and crystals. Plastics in particular are preferred over inorganic scintillators due to their relatily low cost, which makes them easily replaceable and widely available on the market [13].
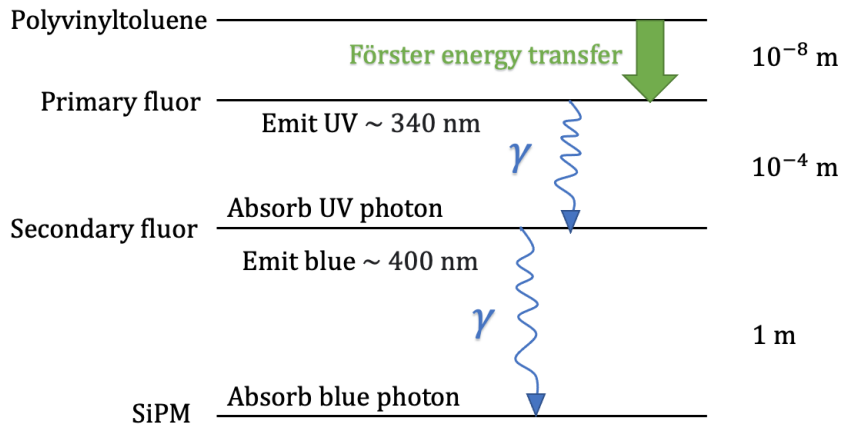
Figure 9: Mechanism of a plastic scintillator. Energy transfer distances shown on the right hand side.

A plastic scintillator consists of a plastic matrix base, in this application polyvinyltoluene (PVT), which is fluorescent in ultraviolet light. PVT can lack stability against aging effects but has a higher light yield than other matrix bases available, making it an ideal scintillation material for this trigger application [20]. Plastic matrices are formed when an organic scintillator

is dissolved in a solvent which is polymerised and can be formed into many different shapes and sizes [13]. An outline of the mechanism of a plastic scintillator is shown in Figure 9. The main purposes of the fluors are to efficiently re-radiate absorbed energy, to increase the total light yield by decreasing the decay time and to enhance the radiation resistance of the scintillator [19].

Förster energy transfer, the transfer of energy from a donor molecule to an acceptor molecule, is possible between the PVT and the primary fluor due to the very small distance between the molecules at this point of the process. After this point, the distances are too large and so energy is transferred via gamma radiation.

The EJ-212 scintillator from Eljen Technology was kindly provided to us by our academic consultant at CERN, in the form of at 10x10x0.2cm tile. This scintillator has the PVT matrix base required for this application, is compatible in a primary vacuum and has a high scintillation efficiency of 10,000 $photons/MeVe^-$, making it the ideal choice for our trigger and its specifications (see section 1.5).
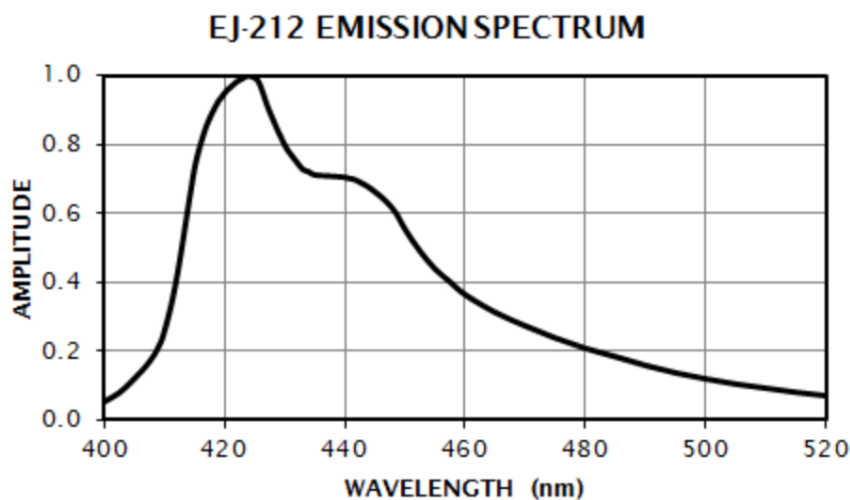
Figure 10: Emission spectrum of the EJ-212 scintillating tile, with a peak in the blue light region at 425nm [21].

With the aid of Figure 10, it is shown that the scintillating tile emits photons at a higher frequency than that of which the SiPM can absorb for maximum efficiency. The SiPM used has maximum detection efficiency at approximately 470nm (see chapter 2.5). Therefore, to improve the efficiency of our design a wavelength shifting fibre was incorporated to bridge this frequency gap.

Furthermore, as the strongest indication of radiation damage is increased optical attenuation at short wavelengths, the long emission spectrum of the EJ-212 is ideal as it provides additional resistance to this damage [21].

2.3 Wave-Length Shifting Fibres (WLS)

Optical fibres doped with wavelength shifting molecules or coated in a wavelength shifting paint are used to transmit signals between the scintillator and a photomultiplier. By converting short, high energy wavelengths of light from a scintillator to longer, lower energy wavelengths, they can more efficiently transmit a signal which meets the specifications of conventional photomultipliers than an ordinary optical fibre. This effect is achieved following the Franck – Condon principle [22]. The WLS fibre operates according to fluorescence from the absorption and emission of photons. The principle states that, during an electronic transition, the nuclei of the molecule or dopant ion do not move significantly, but rather remain in their original positions. This is because the electronic transition occurs much faster than any nuclear motion. As such, when the input photons excite the activator dopants, an electronic transition takes place where the molecule or ion remains in place. Thus, the energy of the electronic transition is conserved and can be used to emit a photon of a different wavelength. This process can occur with multiple dopants and co-dopants to achieve a longer shift in wavelength proportional to the concentration of dopants used. Therefore, a WLS can be tuned to output a signal at a wavelength optimised for any application. For this case, the Kuraray Y-11 WLS fibres were used. According to its specification [23] the Y-11's absorption and emission spectra has peaks at blue ($\approx 430nm$) to green ($\approx 476nm$), respectively. These spectra overlap with the emission spectra of the scintillator used, the EJ-212 ($\approx 425nm$) [21], and the absorption peak of the silicon photomultiplier used, the Hamamatsu S12572-025P ($\approx 450nm$) [24], making it an optimal choice for this project.
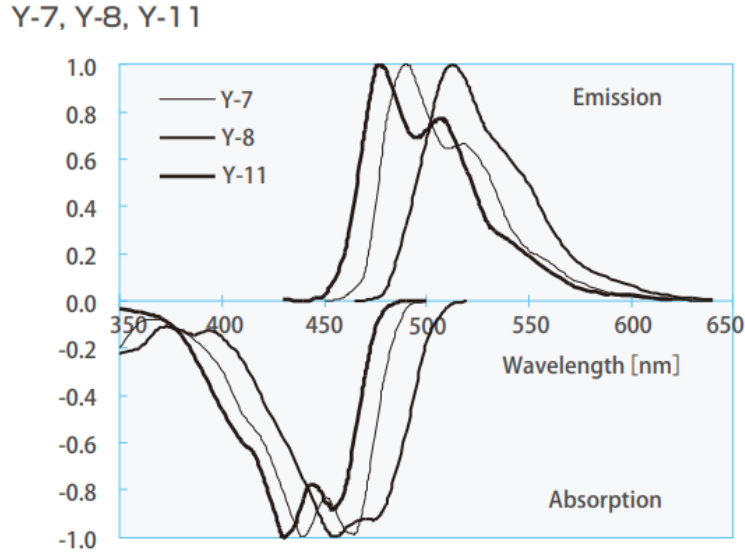

Figure 11: Absorption and emission spectra of the Kuraray Y-11 wavelength shifting fibre (thick black line), showing absorption at $430nm$ and maximum emission at $473nm$ [23].

2.4 Photodetectors

2.4.1 SiPMs

The photons from the WLS fibres must be converted into an electrical signal so that a read-out and analysis can be conducted. As the light intensity from the WLS fibres is so low, photodetectors are used to multiply the current that would have been produced by the light up to 10^8 times. Photomultiplier tubes (PMTs) were used at first, but there are more recent technologies, such as Silicon Photomultipliers (SiPMs), which have several advantages.

PMTs are the most commonly used vacuum electronic device, most often used in particle physics, astronomy, and medical imaging. The first part of a PMT is the photocathode, which is responsible for emitting electrons via the photoelectric effect caused by the incident photons from the WLS fibre. These electrons are accelerated towards a series of dynodes (electrodes), which are each at a more positive potential than the dynode before. The incident electrons knock out surface electrons from the dynode, and thus at each stage, several more electrons are released for each incident electron via secondary emission. It is reasonable to assume a multiplicative factor of 10 at each dynode, which results in a total of $10^5 - 10^7$ electrons per photon. This flux of electrons then reaches the anode, which produces an electrical signal proportional to the photon intensity incident on the PMT.

More recently, SiPMs have been replacing PMTs due to their increased reliability, and a decrease in their size and cost. SiPMs are made up of a dense array of pixels, up to roughly $10^4/mm^2$. One pixel is made up of an avalanche photodiode (APD) that works in Geiger mode and is connected to a polysilicon quenching resistor. The circuitry of the SiPMs is shown in FIG 12. An APD works by setting a high potential across the p-n junction of a semiconductor photodiode, and when a photon is absorbed near this junction, it can cause an electron to be ionized.
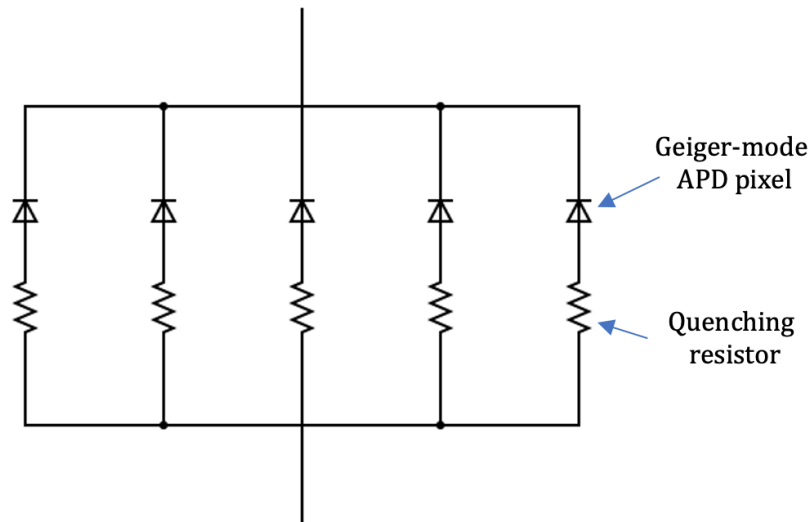
Figure 12: Broken down structure of an SiPM. Five individual pixels of it are shown, each composed of a Geiger mode APD and a quenching resistor.

The APD is biassed above its breakdown voltage so that incoming photons cause an avalanche of electrons. This is what it means for the APDs to be working in Geiger mode. The stronger the electric field, the more ionization, and therefore gain, will occur. This means that for every photon incident on a different APD, there will be a voltage pulse output. These can be superimposed by multiple pixels firing at once, but if multiple photons hit the same APD in too short a time

period, only one of them will output a pulse. This means that APDs are much better suited to low-light environments, which is exactly what this project is testing. In order for the APD to not generate dangerous currents, a quenching resistor is used, which reduces the current and potential difference across the diode after a photon is absorbed. This allows the APD to reset and be ready to absorb another photon.

2.4.2 Dark Current

The APD itself can also randomly form electron-hole pairs that cause pixel avalanches without any outside radiation entering the detector [35]. This is called dark current and is much greater in SiPMs than in PMTs. This means that there will be several false positives; the number of which is proportional to the area and increases with temperature. Two ways to combat this are to lower the temperature in order to decrease the chance of random electron excitation, or to use two SiPMs and look for coincidence readings. Since the chance of a dark current spike is completely random and happens within the SiPM, only looking for coincidence readings greatly reduces the chance of a false positive.

3 Experimental Methods

3.1 Overview

The active section of the detector is made up of a single plastic scintillating tile from Eljen Technology of dimensions $10x10x0.2cm$ and two single-clad Kuraray Y-11 WLS fibres; one attached at the left and the other to the right hand side of the tile. These fibres are of diameter $1.25mm$ and were cut and polished to be the same length as the sides of the tile. An SiPM was connected to one end of each WLS fibre. Using two SiPMs gave us the ability to measure coincidence to ensure each reading of a photon collision was in fact a collision and not simply a dark count or noise. Optical grease was used in between the fibre and SiPM to increase photon detection efficiency. This whole active area, along with the readout electronics, were held together in a plastic 3D printed box design, as outlined in the chapter below. The read-out electronics included resistors and grounding to lessen the safety concerns surrounding electrocution. The circuit was designed so that the voltage and current outputs could be measured independently; all of which is discussed in detail in chapter 3.3. Originally the design was powered by a power supply, however, due to high levels of noise, this was switched out for several batteries connected in series. Testing began using visible light to ensure that the design was indeed light sensitive. Once this sensitivity was confirmed, a radioactive source, Caesium-137, was used to replicate the beamline conditions in CERN's experimental areas. Later on, this beta and gamma emitter was switched out for a stronger source, Americium-241, which is an alpha emitter. Using this source it was possible to gather better experimental data detailed in chapter 4.

3.2 Design of Unit

The design of the unit was primarily structured around three central criteria:

1. Areas of contact between WLS fibre and scintillating tile, and between WLS fibre and SiPM are secure and maximised.

2. The electronics are shielded to reduce danger of electrocution during testing.

3. The unit can be held securely within pipeline, and allow connection of detector to other instruments.

It was decided that the design should be 3D printable to allow for the required level of intricacy. Because there could be no overhangs causing a lack of support to layered filament, any design of the box must be printed in multiple parts that could then be fitted together. Initially the box design was printed in a bottom half and a top half and then just fitted together but there were several problems with this. Firstly, the natural flexibility of the plastic meant that at the join in the middle, the sides were able to bow out slightly. This was not by a large amount, but enough to ensure that the scintillating tile was able to fall out of the 2mm ridge. Secondly, due to the printing process, the hole that the WLS fibre would stick out onto the SiPM would be blocked and the lack of access to it from underneath meant it was extremely difficult to gain access to for clearing. Finally, the box was still much bigger than it needed to be and so there was a lot of empty space and cable lengths were longer than they needed to be (increasing noise in the system). A final design in three separate parts was conceived.
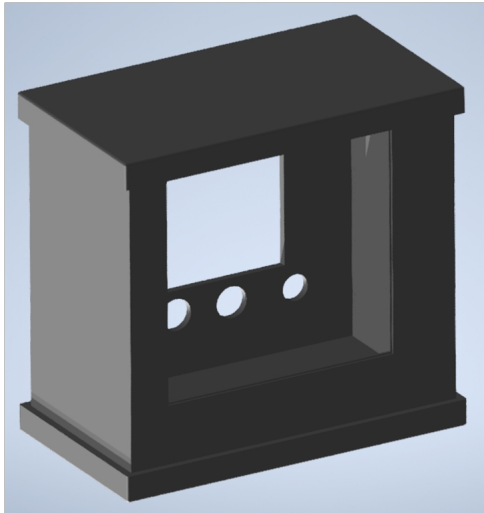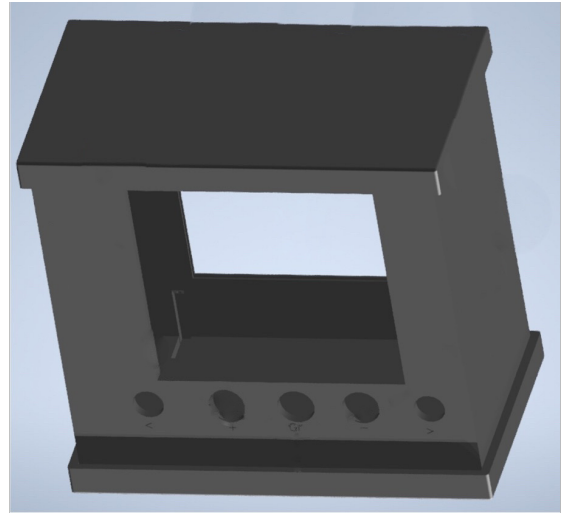
(a) Front of final design   (b) Back of final design

Figure 13: Renders of final segmented box design
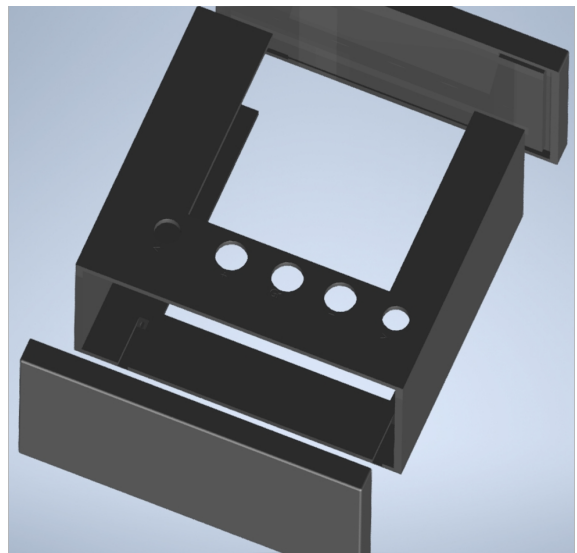
(a) Front of final design   (b) Back of final design

Figure 14: Exploded renders of final segmented box design

Figure 13 shows how the assembled final unit looks from the front and from the back. The large hole at the front is where the scintillator will sit, with a gap at the back of the unit to allow the beam to pass through without further impedance. The veroboard sits at the very bottom of the unit, below the ports; this means that the space of the unit is maximised and it is as compact as it could be. The holes for the ports have also been placed such that the shared ports for each SiPM of positive, negative and earth are roughly equidistant for both, whilst the BNC ports for each SiPM are on the relevant sides, further reducing wire length.

An exploded view showing the three component parts can be seen in Figure 14. The ridges seen in the top and bottom pieces are where the middle part slots in, this prevents bending and expansion of the gap for the scintillator, keeping the tile secure and the WLS fibre firmly pressed to the side. Figure 14b also shows the hole through which the WLF would extend past the tile and onto the SiPM. Shown here zoomed in, the hole can be accessed from the bottom, allowing it to be cleared easily from any blockage formed during the printing process. It also has a 45° angle that prevents problems caused by the slight overhang. Once the SiPM is placed in the gap a small piece of 4mm thickness square plastic can be cut to size and fitted into the ridge below the hole and on the bottom plate to support the SiPM. This also means that the output wiring of the SiPM comes out just above the circuit and therefore length and noise is reduced to a minimum.
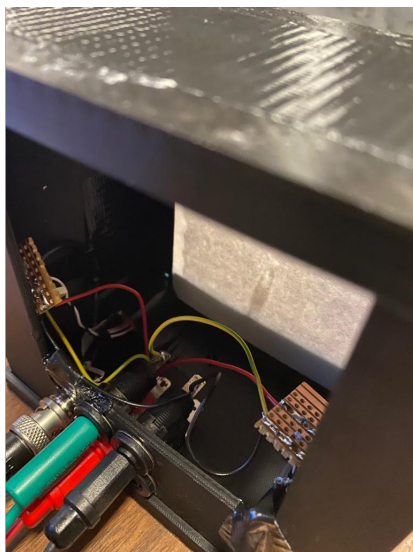

| (a) The SiPM attached in the box | (b) The WLF attached to the SiPM |

Figure 15: Pictures of the SiPM in the final printed box

| (a) The back of the final design tested | (b) The top of the final design tested |

Figure 16: Pictures of the final unit used for testing

Figure 15 shows the SiPM as it is held within the unit, the plastic stand it lies on was cut to size individually for each SiPM (in case of any variation between sides) and super-glued into the box. The SiPM itself was then stuck onto the top of this and held down securely by tape. Optical grease was placed between the end of the WLS fibre and the SiPM so that light was able to easily pass between the two with better efficiency.

As can be seen in figure 16a the model used for testing was an earlier design, the only difference being the hole placement. This meant that during testing, great care had to be taken to keep the unit secure, but it did not affect the results collected as compared to the full unit. Also can be seen is a small piece of paper placed behind the scintillator, this was to try to reflect escaping light from the tile back into the system and hopefully increase efficiency. Figure 16b also shows tape holding down the lid; in the actual unit the lid would be glued down but as access was needed to open it up to perform troubleshooting, tape was used.

3.3   Scintillator-SiPM Coupling

The coupling between the scintillating component, the tile and WLS pairing, and the SiPM is crucial in determining the amount of light being propagated to the SiPM and therefore ultimately effects the overall efficiency of the design. To establish how well these components were coupled, two factors needed to be considered:

- Fresnel Reflections

- WLS Fibre Numerical Aperture

3.3.1   Fresnel Reflections

When a beam light reaches an interface of two media with different refractive indices, part of it is transmitted into the one medium and the other part reflected back into the original medium. This reflectivity and transmissivity at such an interface can be calculated with Fresnel equations [34]:

$$R = |\frac{n_1 - n_2}{n_1 + n_2}|^2 \tag{2}$$

In this design there are several of such interfaces and so the calculation becomes,

$$R_{total} = R_{tile-air} + R_{air-fibre} + R_{fibre-air} + R_{air-SiPM}, \tag{3}$$

where air must be included due to inevitably imperfect mechanical coupling between each component.

Using the refractive indices data from each manufacturer,

- $n_{tile} = 1.58$

- $n_{fibre} = 1.59$

- $n_{SiPM} = 1.55$

- $n_{air} = 1$,

the total reflectivity was calculated to be,

$$R_{total} = 5.05\% + 5.19\% + 5.19\% + 4.65\% = 20.08\%, \tag{4}$$

making the transmittance $T = 79.92\%$.

With the addition of the optical grease, Dow Corning Q2-3067 453G, with a refractive index of 1.47, the reflectivity was be reduced by 0.2%, meaning the final calculation for light transmittance from the scintillating tile, through the WLS fibre with the aid of optical grease, to the SiPM was 81.92%.

3.3.2 WLS Fibre Numerical Aperture

In order to ensure that all the light emitted from the WLS fibre was being collected by the SiPM, geometrical calculations had to be carried out. Numerical aperture (NA) is a value given to describe the range of angles in which a system can emit light and is calculated using the expression,

$$NA = nsin\theta, \tag{5}$$

where n is the refractive index of the active area of the SiPM in this case and θ is the angle at which light is emitted from the edge of the core of the WLS fibre, as shown in Figure 17.
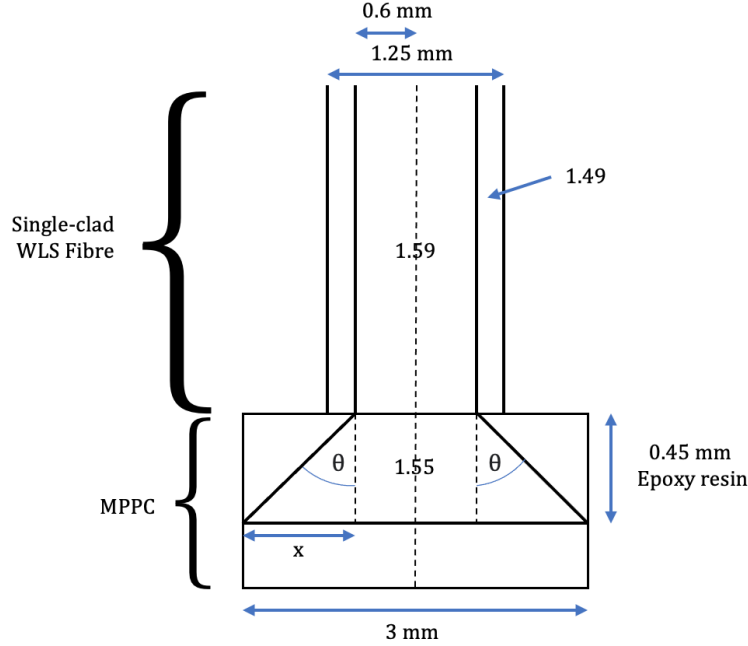
Figure 17: Original schematic of the WLS Fibre coupled to the Hamamatsu S12572-050P SiPM used to calculate whether the SiPM was able to collect all of the light emitted from the WLS fibre (not-to-scale). θ is the angle at which the scintillating light exits the fibre and lands on the $9mm^2$ active area. The refractive index of each component is labelled.

The active area of the SiPM, the multi-pixel photon counter (MPPC), has an epoxy resin of thickness $0.45mm$ which acts as a protective layer. The length x, labelled in the diagram, was calculated using angle formulae to be $0.17mm$, meaning the total diameter of the cone of light emitted from the fibre was $1.54mm$, which fits well withing the limit of $3mm$ of the SiPM surface; these lengths are better demonstrated in Figure 18. As this difference in length was so substantial, no further calculations were required to make up for the likely misalignment of components. As all of the emitted light is collected by the SiPM, the detection efficiency is not affected however, when a ratio of the areas in Figure 18 is taken, the material efficiency is very low, $\approx 21\%$, suggesting that a lot of the SiPM active area is wasted.
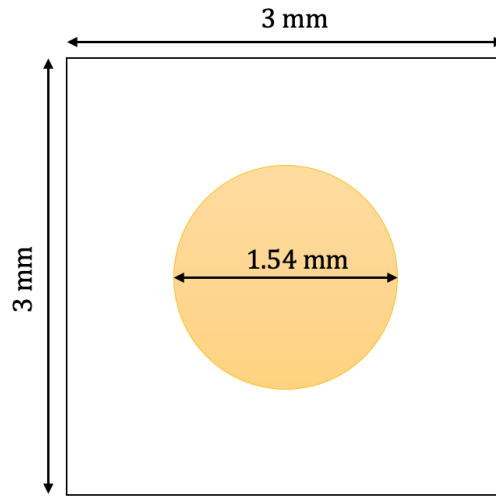
Figure 18: A to-scale diagram showing the size of the cone of emitted light in reference to the active area of the SiPM. It can be seen that all of the light emitted from the fibre is collected by the SiPM.

3.4 Electronics Design

The schematic for the initial design of the circuit was as follows:
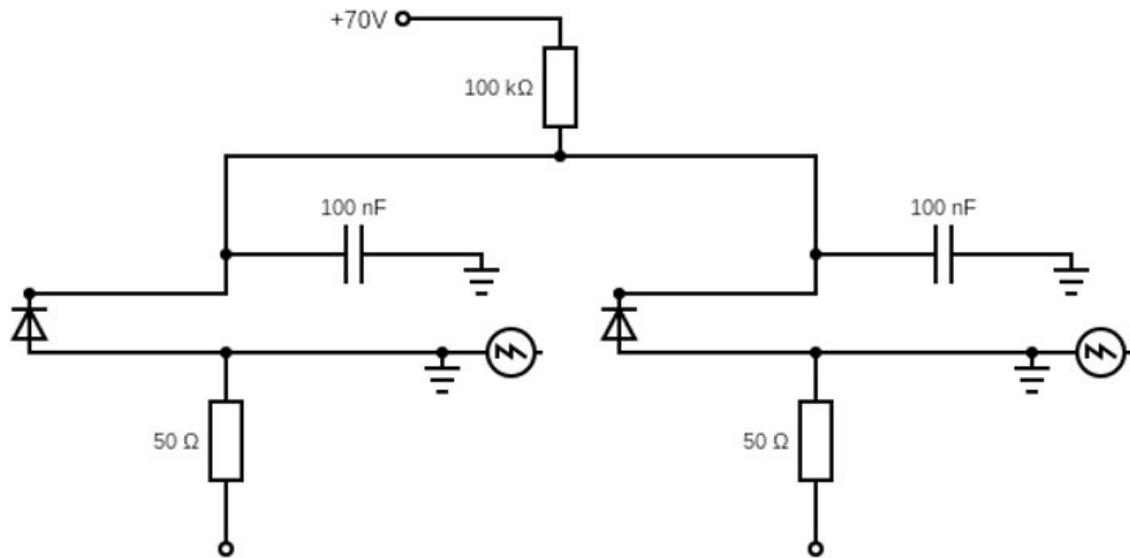
Figure 19: The first circuit design

In figure 19, the 100kΩ after the positive node meant that the current was very low, a safety precaution to reduce risk of electrocution. The capacitor connected to ground helped to absorb fluctuation in the power source. Each SiPM was placed in a reverse bias and had an individual negative node and BNC output so that either the voltage or current variation of each could be measured independently. The SiPM, upon detection of a photon, would induce a spike in both voltage and current. This is translated into a physical veroboard circuit in figure 20.

(a) Shown with SiPMs attached
(b) Close up of circuit itself
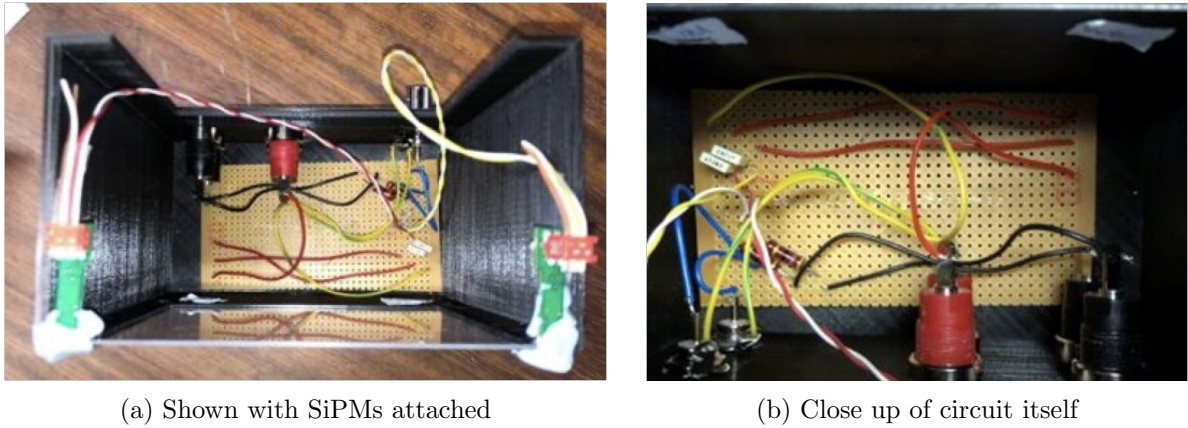
Figure 20: Pictures of the first circuit built

There were several issues with this design that were identified whilst testing. First and foremost, although the capacitor and the oscilloscope are grounded, the circuit as a whole is not grounded. For this reason the negative was instead connected to the ground rail, which while causing the loss of the ability to individually measure current spikes in the SiPMs, did reduce noise. In addition to that the wires connecting the SiPMs, whilst braided to prevent interference, were far too long meaning that any signal rebounding has a long distance to travel and therefore produces a much more delayed and therefore noticeable affect; these needed to be shortened. In addition, the wire connecting the circuit to the BNC port for the oscilloscope was also liable to interference, remedied by the use of a coaxial cable to connect it both to the output of the SiPM and to ground. The largest issue was the output of the power supply; because of the transformer it used, it would give a regular noise pulse that was bigger than most spikes seen, even from dark current. This is shown in figure 21 with the large, repeating pulses roughly every $18\mu s$, caused by the power supply. This was solved by using a battery supply instead. Our final circuit is shown in both design and construction in figure 22.

Figure 21: The noise from the power supply with a maximum amplitude of $2mV$.

(a) Schematic of final circuit design

(b) The assembled veroboard of the final circuit

Figure 22: Pictures of the first circuit built

3.5 SiPM Breakdown Testing

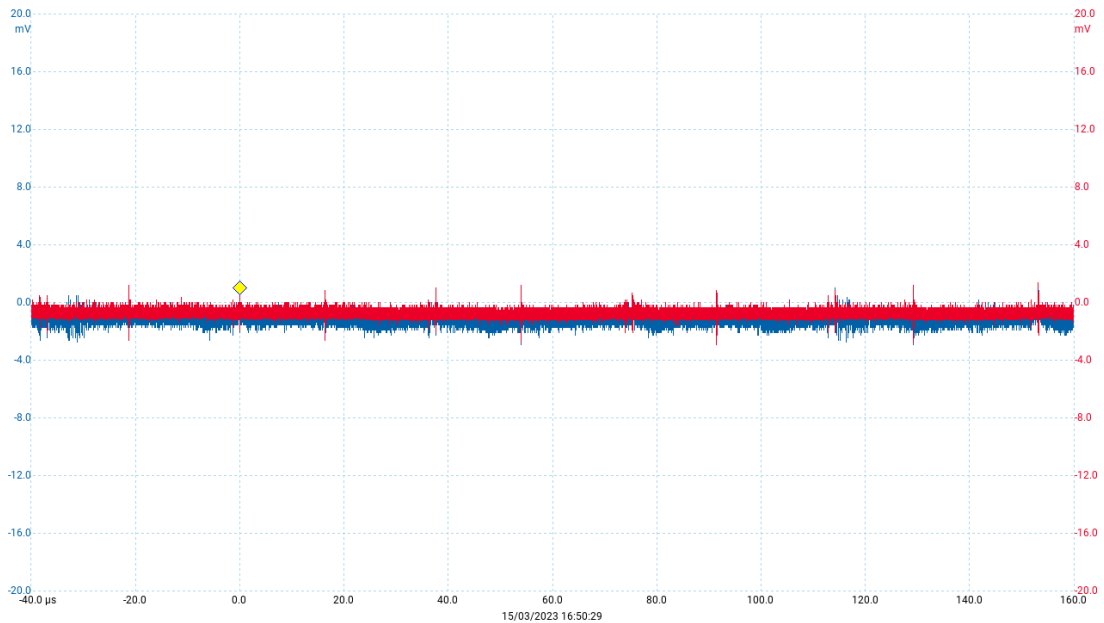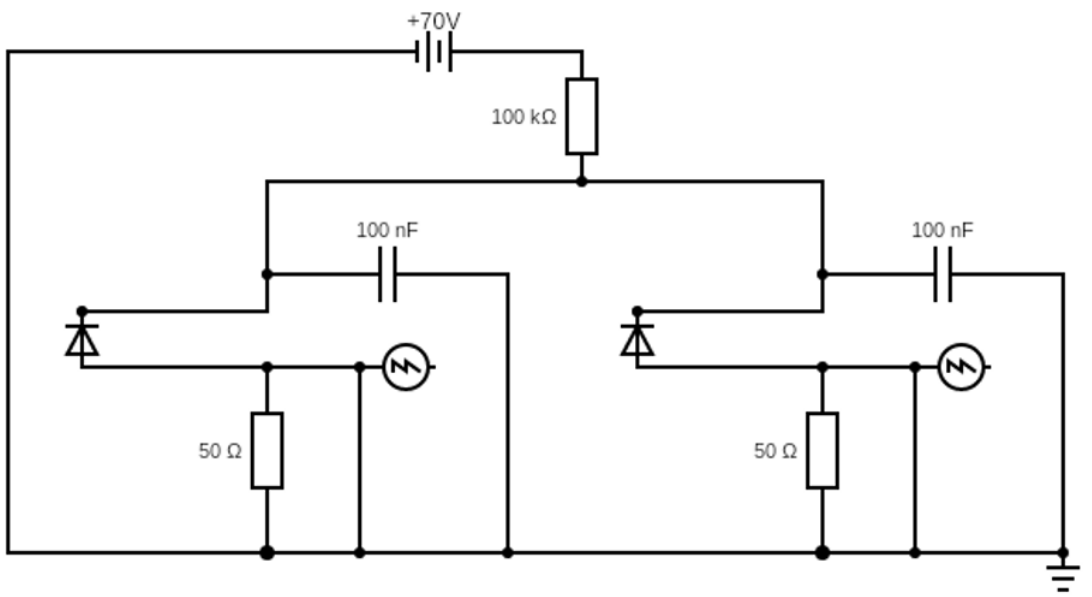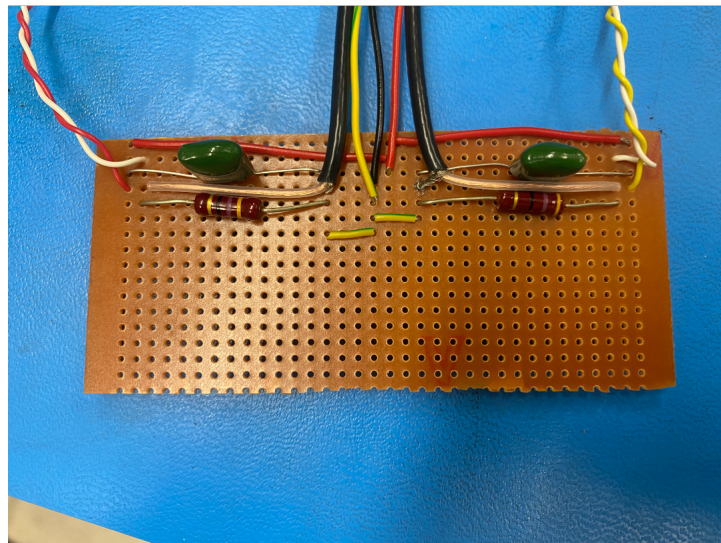This final circuit was placed inside the light-proof box, shown in Figure 23, and connected to a power source. To test the breakdown voltage of the SiPMs by measuring the current through the SiPM, it was necessary to see a sharp increase in the difference in current when the SiPM was exposed to light. To do this, a 1.6mm hole was drilled into the box lid, and the SiPM was held just underneath this hole by blue tac. The hole was covered and uncovered with an opaque sheet to provide a change in light intensity. It was put through this process at a range of voltages in order to find the point of increase. Some code was written to read the current from a Keithley 2000 multimeter. The number of iterations (NOI) of the code, corresponding to the number of data points, was kept at 10 to allow quick testing to find a rough range of the breakdown voltage, but this was later increased to 30 when determining the breakdown voltage more accurately.
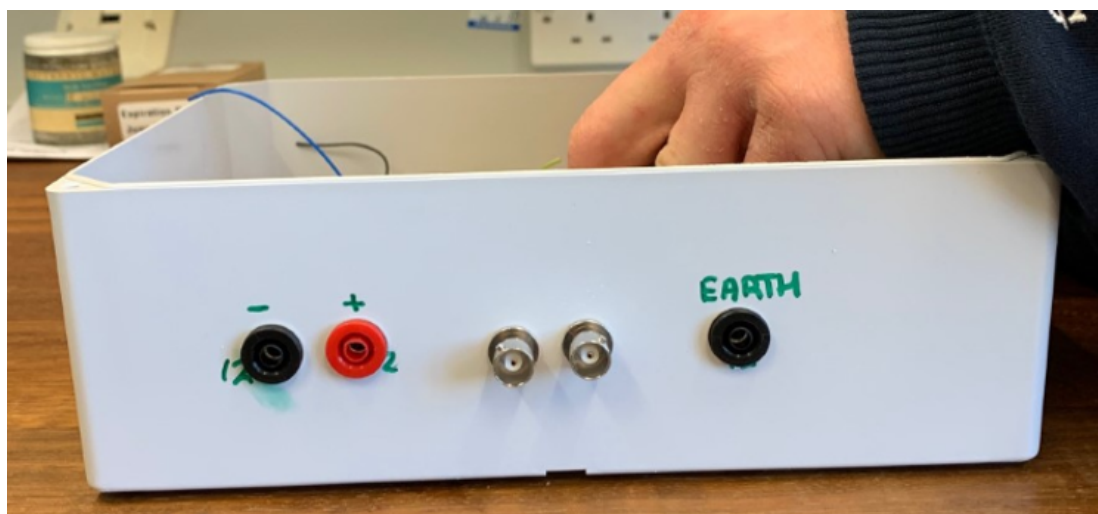
Figure 23: The first box used to house the circuitry and SiPMs. This was what was used to test the breakdown voltage of the first and second SiPM, and where the WLS fibre testing was conducted.

Due to manufacturer uncertainty in the breakdown voltage of any given SiPM in a batch, the behaviour of another SiPM (SiPM2), with a currently unknown breakdown voltage, was measured under the same conditions as the first SiPM (SiPM1), which had a known breakdown voltage. They were both biased at $60.8V$, and the difference in the current flowing through them was measured with the same cover and uncover technique used to initially measure the breakdown voltage of the first SiPM. This allowed an estimate of the breakdown voltage of SiPM2. After this, only SiPM1 was used for testing with the WLS.

The next part of the trigger was now ready to be introduced, which was the wavelength shifting fibre, and this was attached to the SiPM with optical grease. This went through the hole in the box in Figure 23 until it was resting on the SiPM, effectively meaning the vast majority of light that was incident on the SiPM had travelled through the WLS fibre. The WLS fibre was covered and uncovered, using a large, black, plastic bottle as opposed to the black sheet, and the difference in current was measured again, but this time only at $60.8V$, $2.6V$ above the breakdown voltage to ensure optimal SiPM performance at the lowest voltage.

3.6 Dark Current Observation

Now that the circuit had been proven to work with the WLS fibre, voltage was now measured instead of current, as this would allow for the detection of single photons and dark current much

more easily. A picoscope was now used instead of the Keithley multimeter to be able to see the signal in real time. The SiPM was biased at $60.8V$, $2.6V$ above breakdown voltage, and the whole circuit was left in complete darkness under a box and an opaque black sheet to try and detect dark current. This was not detected due to the significant amount of noise from the power supply of around $20mV$. An LED pulse generator was introduced to systematically set the amount of light incident on the SiPM and allow more precise measurement of the behaviour of the SiPM in reaction to light. Figure 24 shows the circuit used to connect the LED to the pulse generator. The bias of the SiPM was increased to $65.8V$ volts, increasing the signal to noise ratio for LED pulses so that better signal envelopes could now be seen. However, the noise was still too high for dark current to be seen.
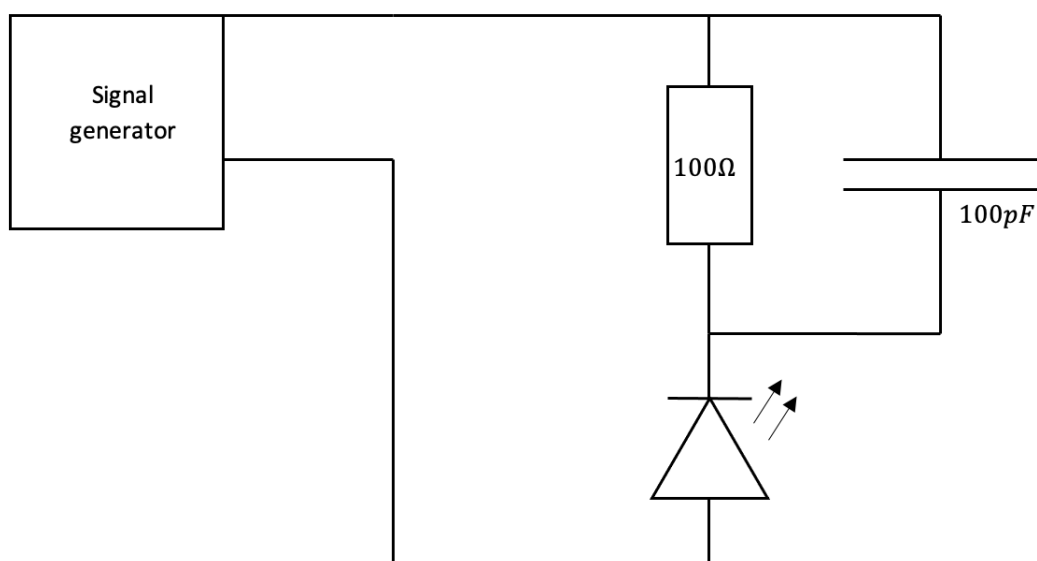
Figure 24: The circuit diagram for the LED connected to the signal generator. This set up was used to test the behaviour of the SiPMs more effectively.

At this stage, it was decided that significant changes needed to be made to the setup to reduce the noise to a level below the expected dark current pulses, which were of the order of a few mV. There were three main possible methods of reducing the noise, which were: using batteries instead of a power source, use of a Faraday cage, and adding an inductor before the circuit. The noise of the set up with the inductor did not decrease sufficiently but using seven $9V$ batteries in series provided a much lower noise of less than $1mV$. Due to time constraints, the Faraday cage was not implemented as the signal-to-noise ratio was sufficiently high for dark current peak distributions to be obtained via Python code. This code was structured to only select peaks from dark current and exclude any noise peaks by running checks such as only selecting peaks above a certain height above the signal average, only selecting one peak within a certain time window either side of the highest peak in that window, and ignoring peaks where there were negative troughs within a small time frame either side of the peak. These checks were decided upon by attempting to describe the behaviour of dark current peaks and noise pulses, which can be seen in Figure 21. The full code can be found in the Appendix A.1.

3.7 LTspice Simulations

Once it had been confirmed that our prototype was indeed light sensitive, and before testing it with a radioactive source, simulations were produced using LTspice, an analog electronic circuit simulator computer software, to confirm that our design would pick up a signal, to have a picture of what that signal would look like and for troubleshooting purposes. These simulations involved recreating our circuit digitally using components available on the software.
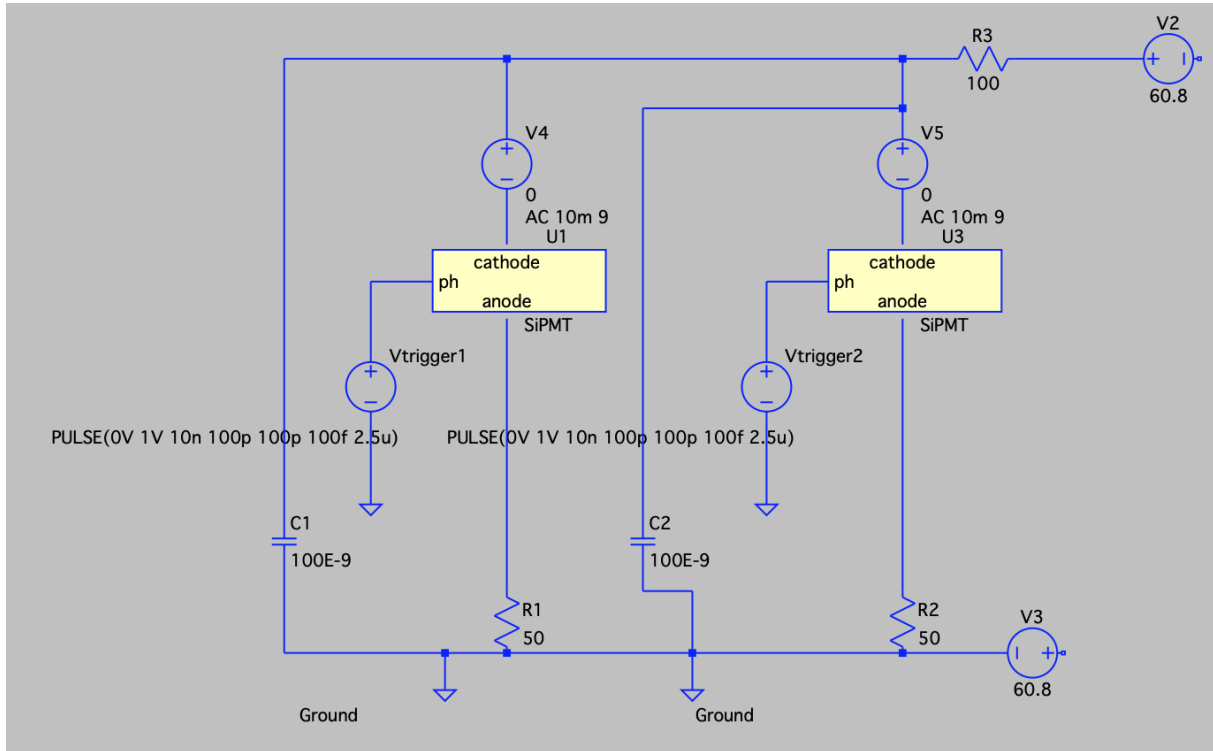
Figure 25: The circuit, built with LTspice software, used to simulate the first prototype measuring individual photons. Note the two "SiPMT" modules replicating the effect of our SiPMs.

A SiPM attachment , provided by David Cussans, that was designed to simulate a single pixel of our SiPM (Hamamatsu S12572-050P) breaking down was used in the simulated circuit. There is an extra "trigger" terminal in the simulation which does not exist in the real circuit; its purpose is to trigger a simulated pixel to fire. The the oscilloscope reading produced by the simulation is shown below. These readings were used as a guideline to identify whether our circuit was in fact working as it was expected to.
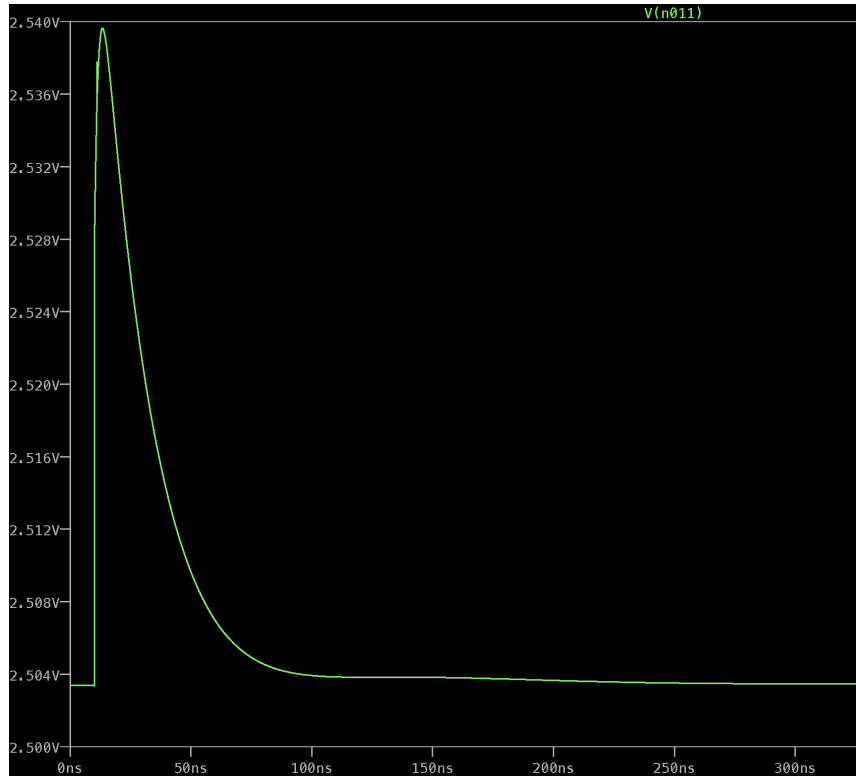
Figure 26: The oscilloscope reading produced when the circuit design was run. This represents a single pixel avalanche.

As shown in Figure 26, the simulated oscilloscope image follows a saw-tooth pattern. This shape is typical of an electron avalanche, as described in chapter 2.1. There is a sudden, sharp increase followed by an exponential decrease in voltage, depicting a photon colliding with the scintillator, ionizing an electron which goes on to ionize other electrons i.e. causing an avalanche. This reading could be used as an approximate reference for when testing began on our design with a radioactive source; although accepting that the voltages and timescales could vary widely from this reference.

3.8 Testing with a Radioactive Source

To test the main functionality of the device it was pertinent to determine whether it was able to detect particles. This was achieved by exposing the detector's scintillator tile to a radioactive source and observing a change in counts recorded by the SiPM using an oscilloscope. It was hypothesized that the count rate would increase proportional to the amount of radiation the tile was exposed to. Therefore the more active the source of radiation, the larger the change in pulse distribution was likely to be, due to increased tile scintillation. The sources used were: Caesium-137, a beta and gamma emitter with decay energies of 0.5120 MeV and 0.6617 MeV respectively [36]; and Americium-241 an alpha emitter of decay energy 5.486 MeV [37]. The Caesium-137 source was proposed to be used initially. In the case that no more pulses were detected, the Americium-241 sample was to be used due to its increased ionising capability. The device was biased with an increased voltage of 68.7V and the picoscope was set to trigger on simultaneous A and B channel avalanches at levels between 2 mV to 3 mV, depending on the amount of noise observed during measurement. This was done with and without the Am-241 source present.

4 Results

A series of results were taken, culminating to identify whether the presence of a radioactive source would increase the particle count rate measured by the detector. Firstly, an estimate for the breakdown voltage of our SiPMs was conducted. This was necessary, as the SiPMs had to be biased a couple volts over their breakdown voltage to work optimally [9]. Once this was known, the dark current had to be measured accurately, before finally using the source to measure the radioactivity passing through the tile.

4.1 Calibration

The first measuring device used was a Keithley 2000 multimeter, which was used to determine the breakdown voltage of the SiPMs used. The SiPM was exposed to an increase in light intensity, and the increase in current through the SiPM was measured against the potential difference across the SiPM. The measurements from a wider range of voltage are shown in Figure 27 (left). The breakdown voltage was calculated from a small section of this data, taken to be just after the initial change in increase of current, located by the intersection of the gradient of the first five and last five points of the graph in Figure 27 (right). This gave a value of $58.2 \pm 0.5V$ for the specific SiPM. The error was taken to be the range for which the gradient lines were not touching the points.
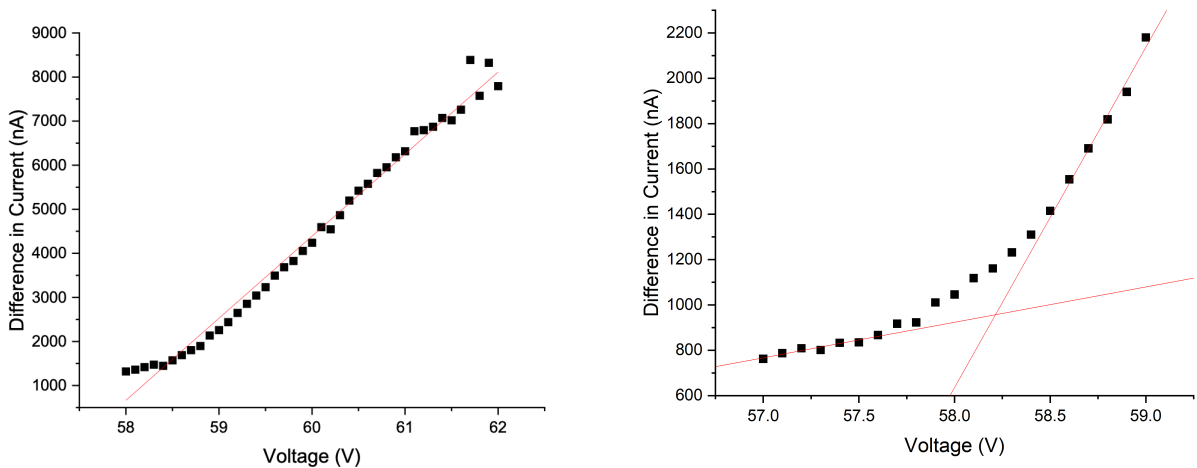
Figure 27: The increase in current through the SiPM when it was covered and uncovered, plotted against the potential difference across the SiPM over a wide range (left). The breakdown voltage as estimated by the intersect of the two lines before and after the first change in increase of current, shown by the red lines (right).

Figure 28 shows the vast difference between the two SiPMs tested, with an increased change in current of 34.3%. Using data from Figure 27 (left), which reached the same average increase in current at $61.9V$, $3.71V$ above breakdown, so it can be estimated that the second SiPM had a breakdown voltage of $60.8 - 3.71 = 57.1 \pm 0.5V$.
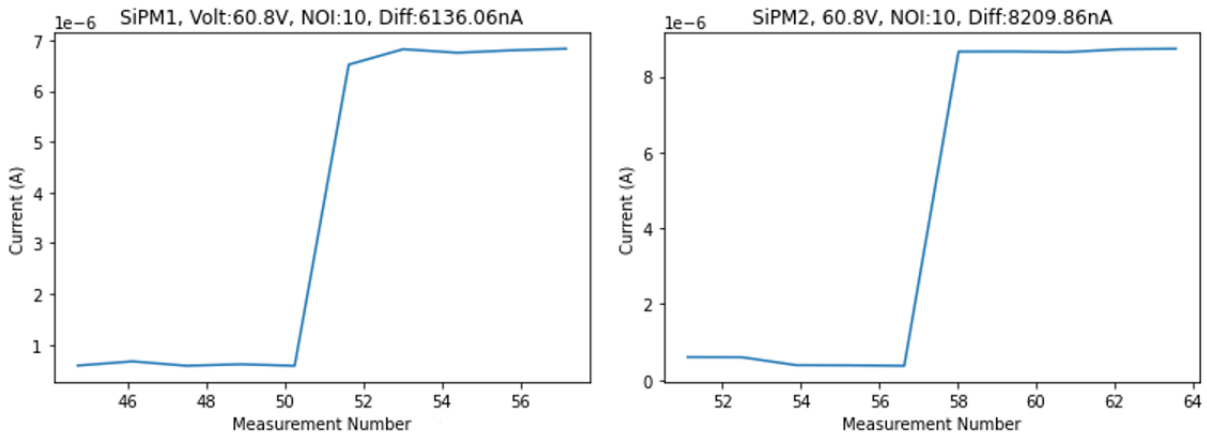
Figure 28: Graphs of current through two different SiPMs when each was covered and uncovered, with the increase corresponding to when they were uncovered.

After this, with the WLS fibre attached to the SiPM the change in increase of current with the WLS fibre increased by 16.7% to $5008nA$ compared with the increase without the WLS of $4291nA$. The current through the SiPM while constantly exposed to light with and without the WLS fibre was also measured, and the WLS fibre increased this by 196%. These plots are shown in Figures 29a and 29b.
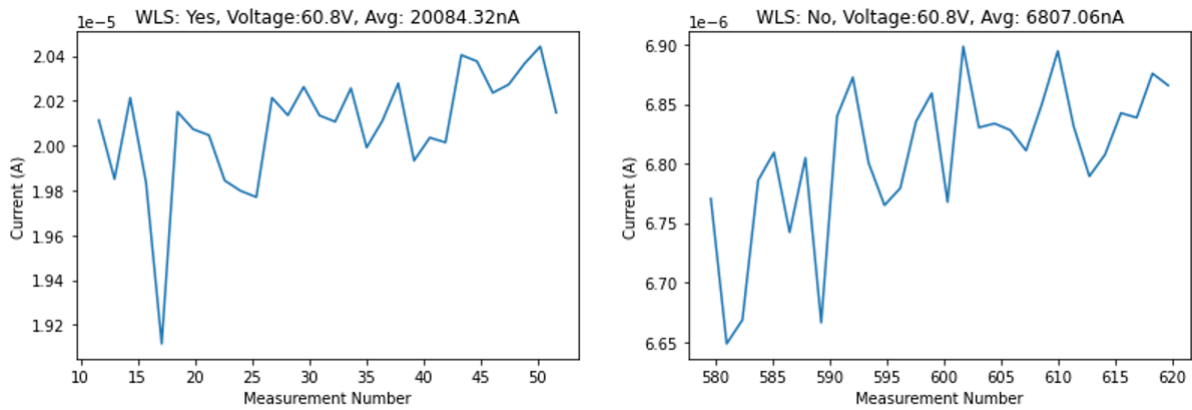
(a) Current through the SiPM with the WLS fibre connected.

(b) Current through the SiPM without the WLS fibre connected.

Figure 29: Graphs of current through the same, uncovered SiPM when the WLS fibre was present and not present.

4.2 Dark Current

The first single-pixel avalanches were observed using the picoscope with the batteries, which were presumed to be dark current pulses occurring randomly at each SiPM, simply due to their separation. Further testing done to determine whether the pulses observed in Figure 30 were in fact single-pixel avalanches. A histogram of pulse height frequency was made to see the distribution of these pulses and can be seen in Figure 31. This histogram was constructed via Python code which can be found in Appendix A.1. This code excluded peaks found in noise pulses such as the pulse on the right hand side of Figure 32. Pulses were more frequent for almost all values on channel A than channel B, with both channels showing an increase in frequency at roughly double the peak value of the most frequent peak value, for example 1.2mV to 2.5mV for channel B. This plot was one of a set made from several time periods.
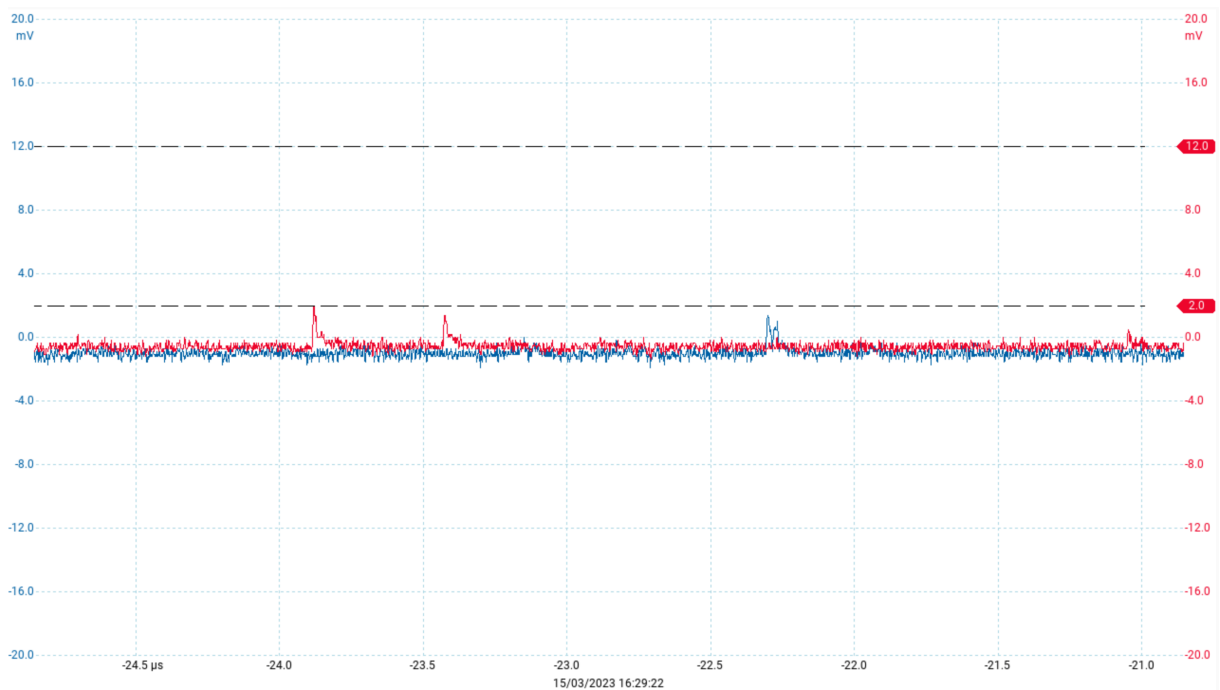
Figure 30: A screenshot of the picoscope readings from measuring two SiPMs in a dark environment with separate spikes.
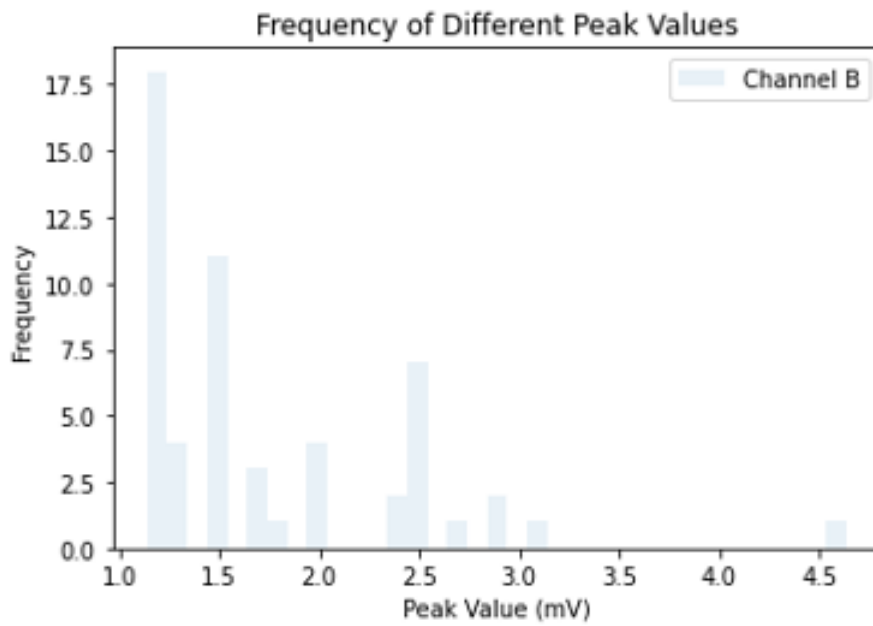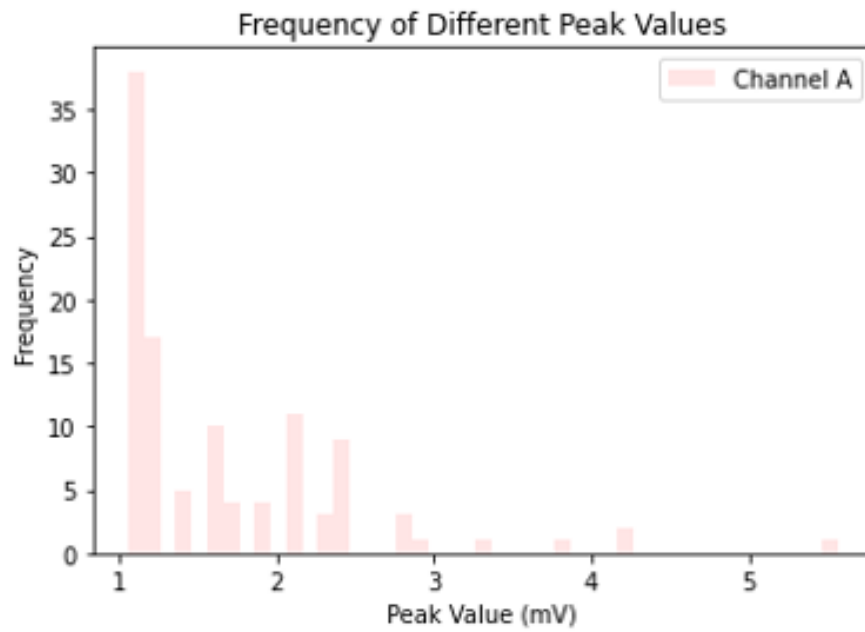
Figure 31: Histograms of peak value frequency for two SiPMs left in darkness over a $20\mu s$ time period.
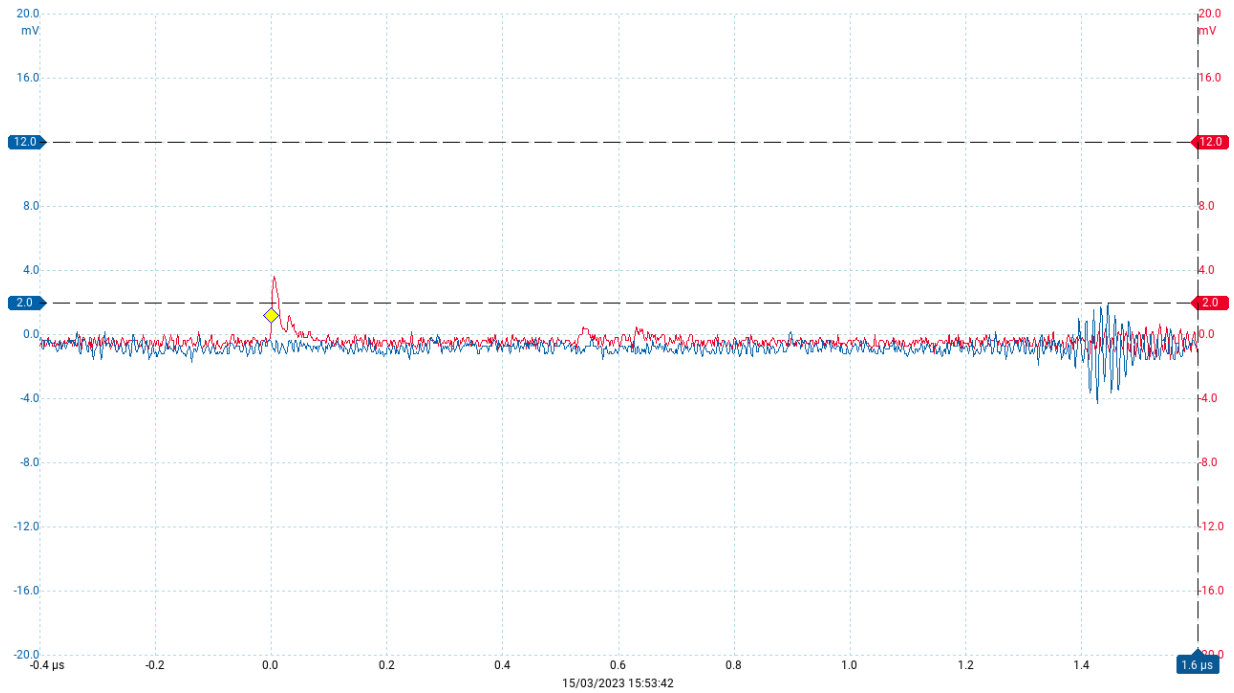
Figure 32: A screenshot of the picoscope from measuring two SiPMs in a dark environment, showing a dark current spike with the yellow diamond set as the trigger level $(1.5mV)$ and a noise pulse on the right hand side.

To observe whether the SiPMs would fire in tandem if they both received light, an LED attached to a pulse generator was placed in front of both SiPMs. A 100ns pulse of 2.5V was sent and the outputs of the LED and both SiPMs were recorded in Figure 33. It was shown that both SiPMs, with a short delay after the pulse, reacted very similarly to each other.
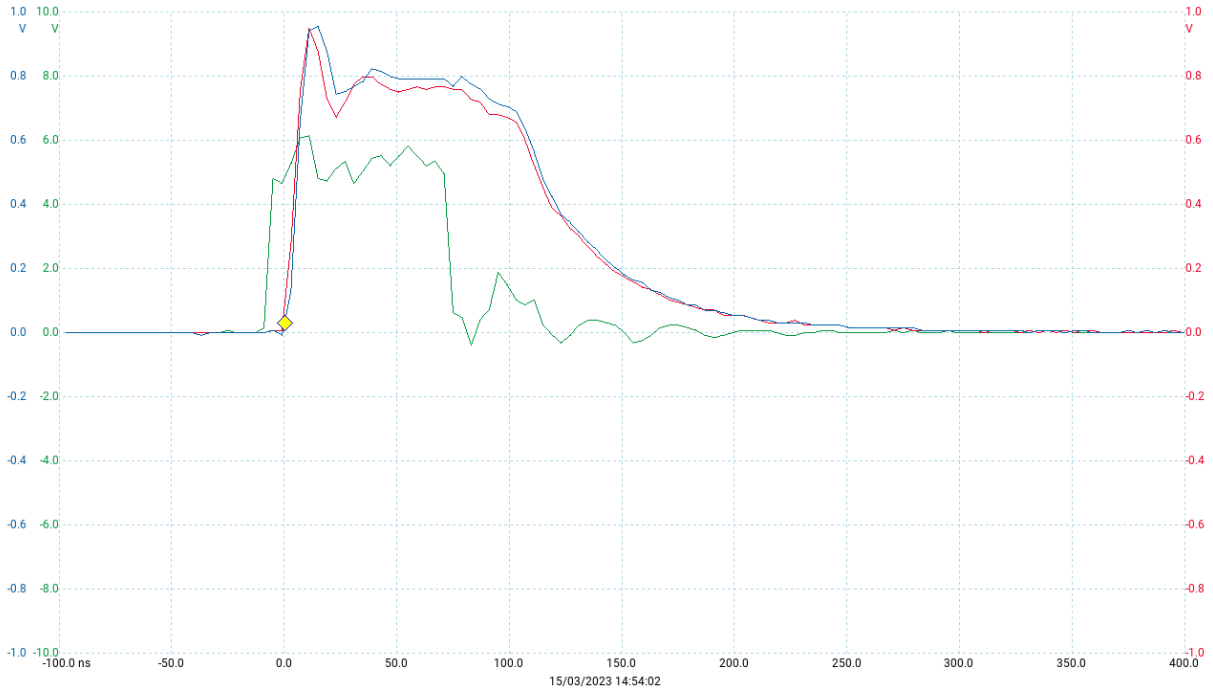
Figure 33: Picoscope signal from the pulsed LED, green, and both SiPMs, red (Channel A) and blue (Channel B), in a dark environment.

4.3 Radioactive Source Data

No visible change was observed using the Cs-137 source, therefore the Am-241 source was used under the supervision of David Cussans. With the Am-241 source present, there was an increase in frequency of higher magnitude pulses compared with no source. Examples of peaks in coincidence, most likely as a result of the source causing scintillation, is shown in Figure 34. A lone peak can be seen after the peaks in coincidence, which was most likely dark current.
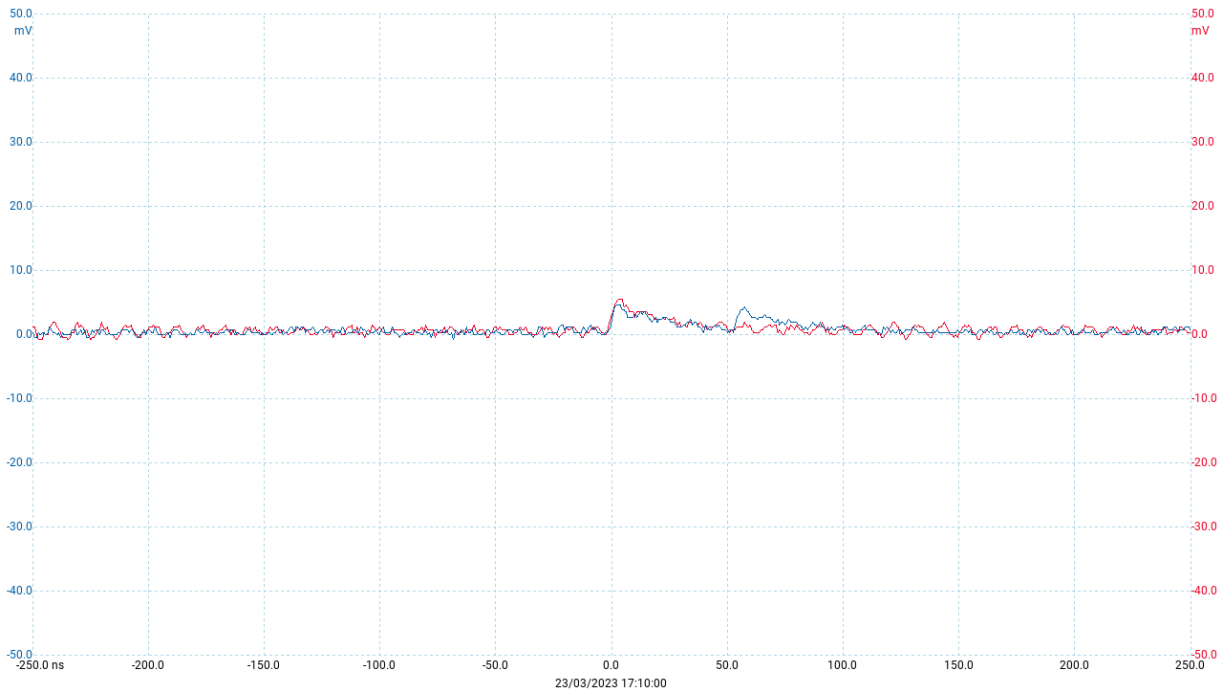
Figure 34: Picoscope readings triggering on channels A (red) and B (blue) simultaneously at 2.5mV.

From Figure 34 it can be noted that there was an increase in noise observed within the pulses recorded to roughly 2mV. This was characterised by the superposition of a sinusoidal function among the signals recorded.

From the no-source and Am-241 source data, a histogram was produced in a similiar fashion to the $20\mu s$ dataset, observing the full range of waveforms recorded. This data was then normalised in order to enable a comparison between the two sample sets of differing sizes in Figures 35, 36 and 37. This was done due to vastly differing data set sizes between the data used for Figures 35 (7000 values) and 36 (2300 values). The original file size for both was intended to be 10,000 waveforms, however due to file corruption on the final day of testing, only the given number of values were retrieved for each sample.

Above $6.0mV$, there were 24.2% compared with 22.0% of pulses for channel A and 32.0% compared with 10.45% for channel B. There was also a decrease in the percentage of the lowest two pulse heights from 34.6% to 32.3% for A and from 39.2% to 22.3% for B. This was taken to be evidence that there was an increase in counts for values in a higher voltage boundary due to the presence of a radioactive source near to the device. It was observed from these histograms and an analysis of the bin spacing in python, that an even spacing of $0.40 \pm 0.01mV$ occurred between filled bins of data, regardless of bin width.
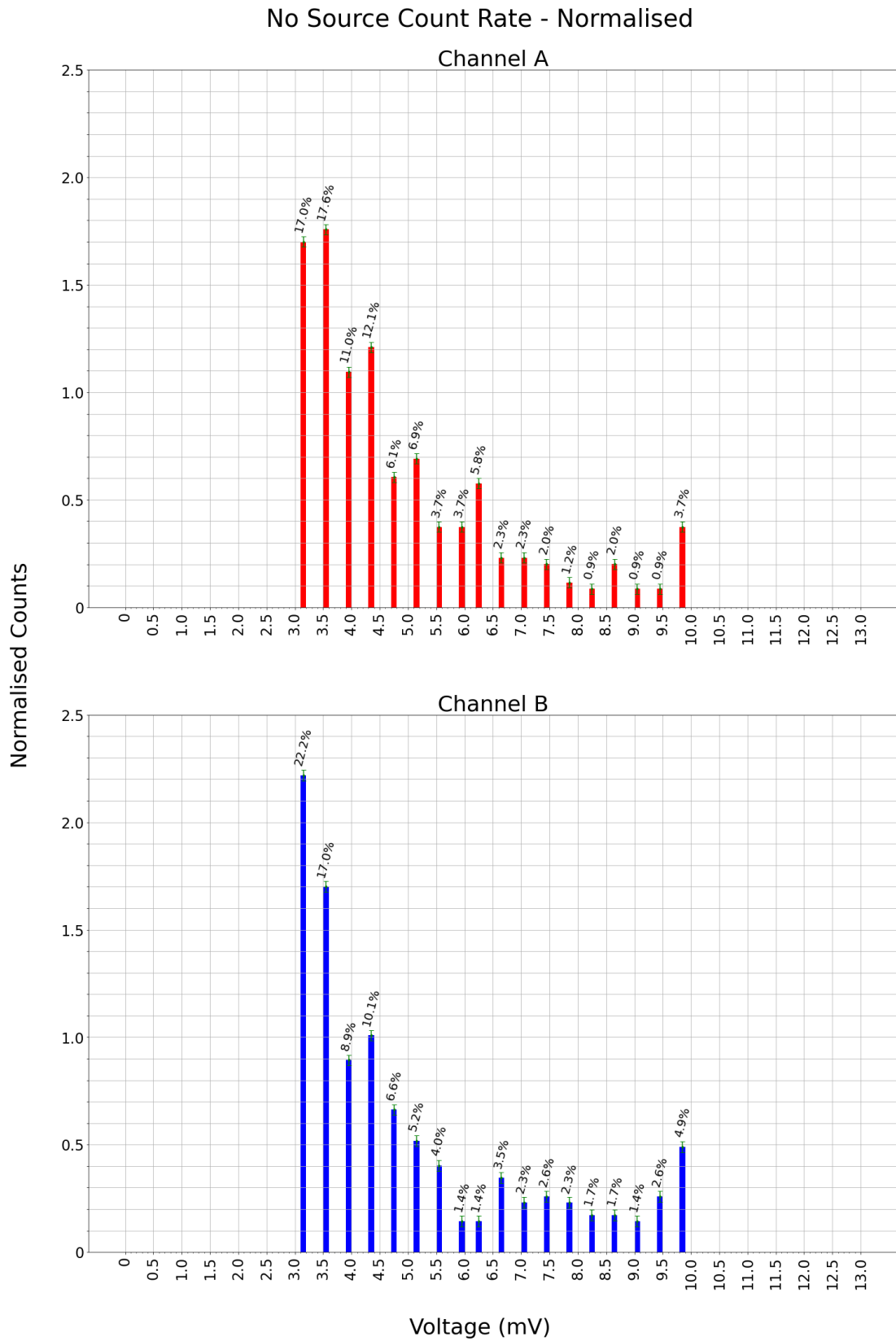
Figure 35: A histogram plotting the normalised coincident counts of the device for 7000 readings when no source is present. The error on the mean of each bar is displayed in green and recorded as 0.0220. The percentages over each bar show its contribution to the total dataset.
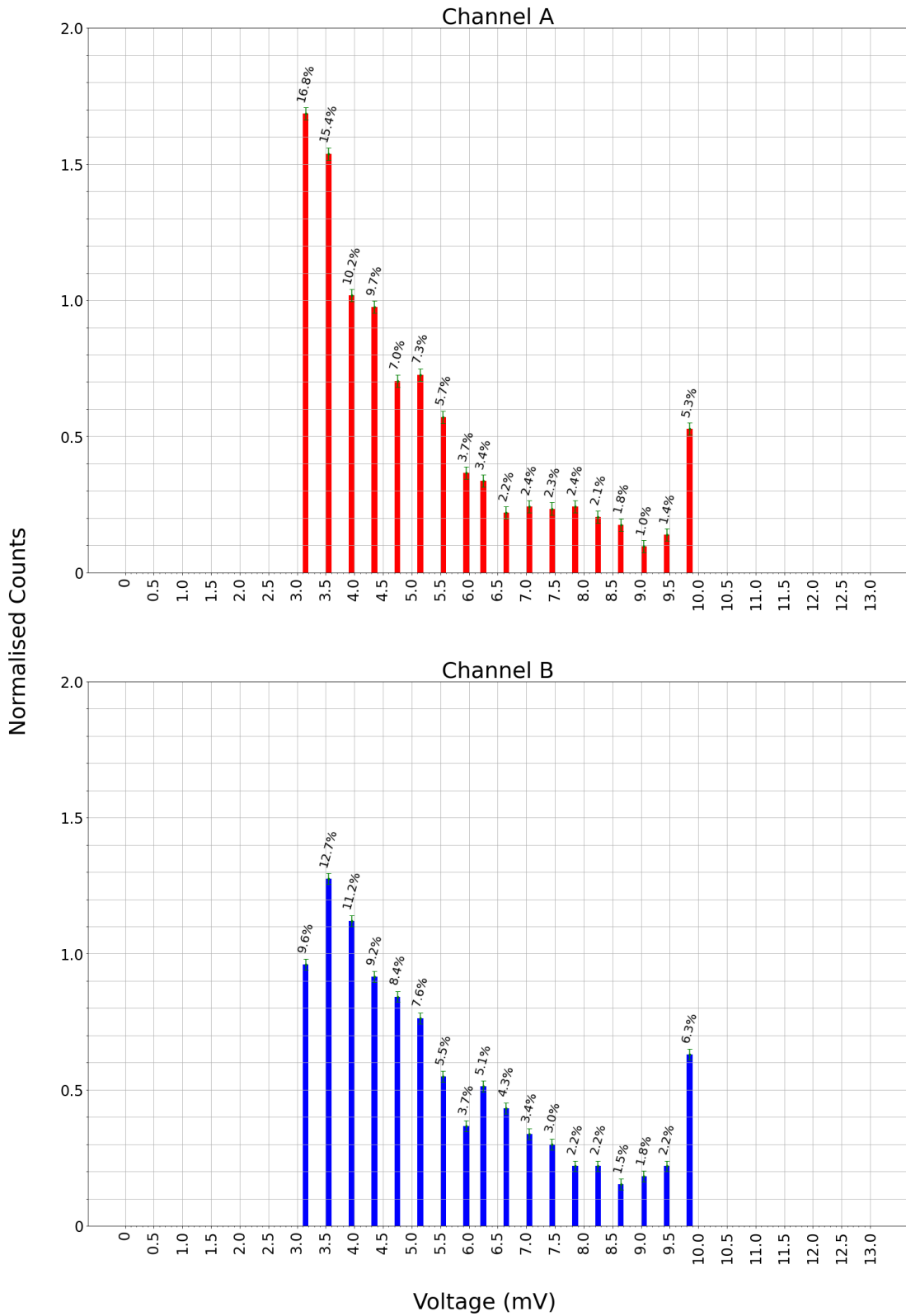
Figure 36: A histogram plotting the normalised coincident counts of the device for 2300 readings when exposed to an Americium-241 source. The error on the mean of each bar is displayed in green and recorded as 0.0226. The percentages over each bar show its contribution to the total dataset.
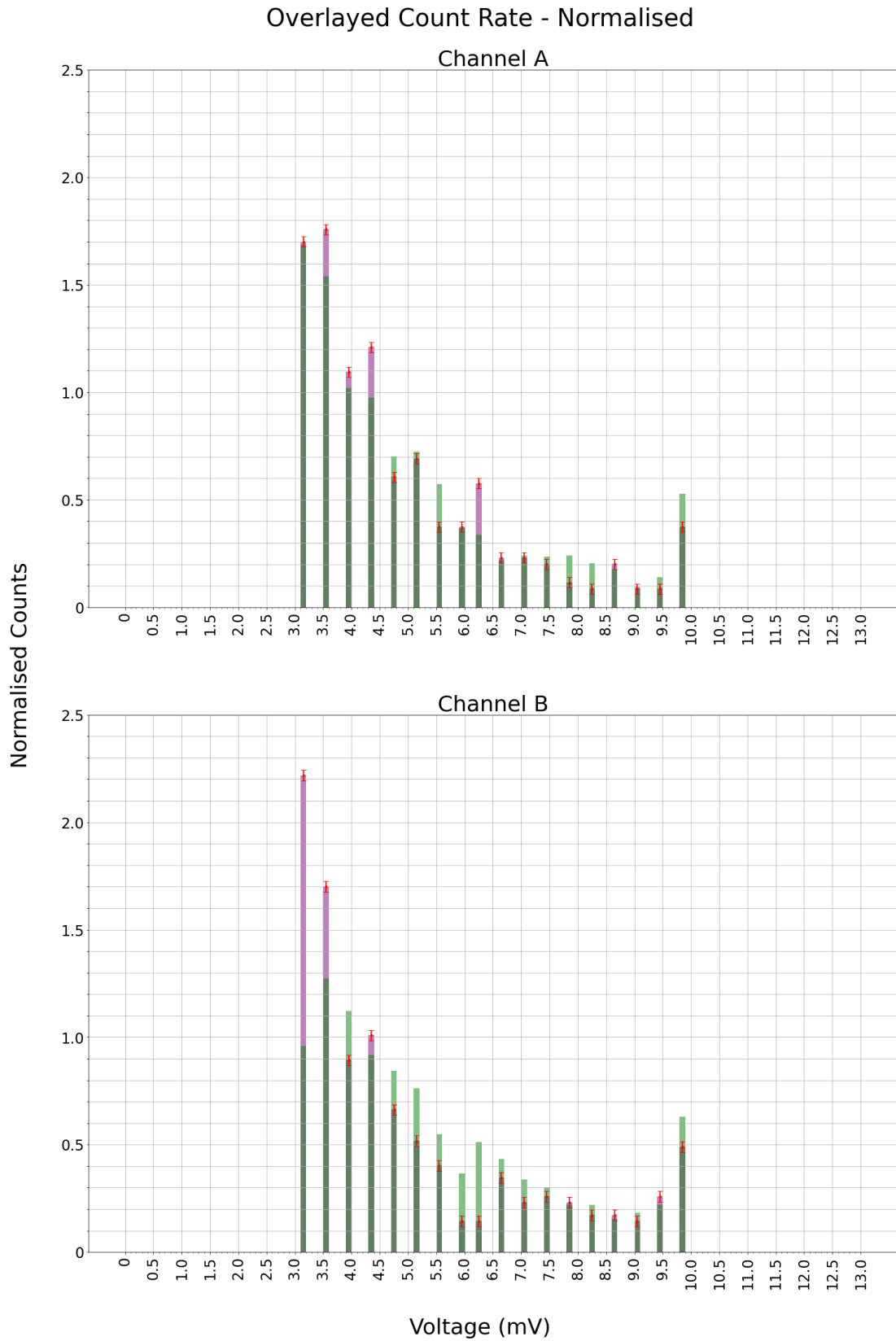
Figure 37: The overlayed histograms of Figure 35 and 36. The combined error is displayed at the no-source value level in red. Purple bars imply a larger count value for the no-source data and light green imply higher values for the Am-241 data in their respective bins. Dark green represents overlap between the two histograms.

5 Discussion

5.1 Efficiency

Our Americium-241 source has a measured total count rate of 23,200 particles a second. Almost all of these particles are $^4_2\alpha^{2+}$ with an average energy of 5.486 MeV. Considering the proportion of these particles that hit our scintillator, given the source is placed 0.5cm off of the tile. Which means that the number of particles hitting our scintillator per second n is:

$$n = (0.09)^2 \times \frac{23200}{4\pi(0.0045)^2} = 7378 \tag{6}$$

The scintillator will produce 10,000 photons [21] per MeV, so each alpha particle will produce 54,860 photons. We want to consider how many of these photons will leave the tile from a side that is attached to a WLF:

$$n = 54,860 \times \frac{\text{Surface area of two edges}}{\text{surface area of tile}} = 54,860 \times \frac{200}{20400} = 537.628 \tag{7}$$

The WLF we used has a 3.1% trapping efficiency, and given that we lose 18.08%, as shown in 3.3.1, we now find that only an average of 13.65 photons reach the two SiPMs per alpha particle. The SiPMs have a time resolution of only $250ps$, but the picoscope would measure waveforms for 500ns after a trigger, so we can consider the 'relaxation time' of the system to be $500ns$. This relaxation time was only present as it allowed a way of taking data to ensure that waveforms with a guaranteed coincidence peak were recorded, but this was for ease of analysis and is not necessary for final implementation. In the final trigger, this relaxation time would not be present and instead the SiPM time resolution of $250ps$ would be the limiting factor. We can assume each 'packet' of photons to all arrive in this time so that each alpha particle only produces one spike. We can model the chance of another packet arriving during this time via a Poissonian equation [9]. In one second there will be 7378 relax periods, so we can find the probability of another packet hitting during one of these periods:

$$\lambda = 7378 \times 500 \times 10^{-9} = 3.689 \times 10^{-3} \tag{8}$$

$$\text{P(k=1)} = \lambda e^{-\lambda} = 3.689 \times 10^{-3} \times e^{-3.689\times10^{-3}} = 3.675 \times 10^{-3} \tag{9}$$

$$\text{Number of particles missed per second} = 7378 \times 3.854 \times 10^{-3} = 27.1 \text{ or } 0.37\% \tag{10}$$

This means that our coincidence spikes should on average be the height of 6.83 photons, as the packet is split between the two SiPMS. Factoring in relax time, we should correctly detect 99.63% of particles. With the SiPM relaxation time taken as the limiting factor instead of the trigger, the efficiency would be above 99.9% as set out by the client. In general the photon efficiency of our system is 0.012%, but for high frequencies there may be problems caused by the relaxation time of the SiPM as shown below. The maximum frequency possible would be 2×10^6Hz as at that point the maximum amount of relaxation times per second would be reached.

Frequency(Hz)	Percentage of particles lost
10^3	0.05%
10^4	0.50%
10^5	4.76%
10^6	30.33%

Our data showed that the voltage was quantised into 0.4mV amounts, with coincidence spikes being of the magnitude of 3mV. This would correspond to an average of 7.5 photons hitting each SiPM per detected particle - very close to our predicted model of 6.83, correlating to an error of 9.81%.

5.2 Data Evaluation

The breakdown voltage of the SiPM1 tested was determined to be $59.2V$, and the SiPM2's breakdown was estimated to be $57.1V$, which both fit in the range of values provided by the manufacturer, $65 \pm 10V$, for the specific SiPMs used as detailed in Appendix section C.

With the introduction of the WLS fibre, the change in increase of current when covering and uncovering was 16.7%, but 197% when measuring the current flowing when the system was uncovered. This is expected, as the WLS fibre emits light of a wavelength closer to the semiconductor band gap in the SiPM, so more of the ambient light in the room is converted to the ideal wavelength of $476nm$. This means more of the light can excite electrons from the valence band to the conduction band more efficiently.

The observation of dark current was first seen with batteries as this reduced the noise levels to allow what were thought to be below single-pixel avalanches. This was because the highest frequency of pulses was at just above $1mV$ for both SiPMs, and then there was a slight increase in frequency at around double this pulse height, but there were still significant significant numbers of pulses at heights in between. At the time, the variation in background noise was thought to account for the deviation from the expected pattern of the largest number of pulses occurring at integer multiples of the most common peak height. This would be the expected distribution for perfectly quantised outputs of the SiPM. This was later proven wrong, when the tests were conducted by triggering measurements when both channels were above the threshold.

Both channels' peak height distributions were changed by the presence of the source, with a smaller percentage of low height peaks and a higher percentage of large height peaks. This was most likely due to the increased amount of scintillation occuring in the tile caused by the alpha particles given off by the source. This would cause more photons to be released at once, which all hit the SiPM at the same time contributing to a higher peak from multiple pixel avalanches. Channel B was much more affected by the presence of the Americium source, with a three times higher increase than A and a five times lower decrease than A. This was because only one side of the tile, channel B, had the WLS fibre completely in contact with it. The other side of the tile, channel A, was likely touching no more than a third of the fibre, because due to 3D printing issues the fibre could not fit down its original hole and so was the top of the box was taped together to compress it such that the WLS fibre was touching the tile for some part of its length. This would have reduced the transmission efficiency between the tile and the WLS fibre.

It was observed from these histograms and an analysis of the bin spacing in python, that an even spacing of $0.4mV$ occurred between filled bins of data, regardless of bin width when below 0.01 mV. This led to the conclusion that a significantly smaller single photon avalanche peak is found at $0.4mV$, not $1.1mV$ as previously thought, when the device is at a biased voltage of $68.7V$. It is unfortunate that the noise was increased in the room where the source was tested, as this restricted the trigger from being below $3mV$ as otherwise it would have been triggering on noise instead of coincidence peaks. The source of the additional noise during the testing with the Am-241 source was believed to originate from nearby radio towers and the change in location of the device from the lower floors of the building to the fourth floor, where less shielding is present.

The delay in the response time of the SiPMs to the LED pulse was presumed to be the lag time between the direct signal to the picoscope and the time taken for the signal to reach the device via light emitted from the LED, processed by the device and sent to the picoscope via BNC cables. This was of the order of 10ns as shown. The slow decay of the SiPMs' signal recorded was presumed to be the relaxation of the LED following its electroluminesence.

5.3   Limitations

Despite our results, some factors that limited the experimental processes performed must be considered.

The scintillating tile, WLS fibre and SiPMs were all provided to us from academics. It would have been of interest and beneficial to the project to test different variations of each component to assess their capabilities, but due to the fact that such components can only be ordered from suppliers in bulk, it was not cost effective to do so and hence those provided to us were the only materials ever used for testing.

Furthermore, through testing it was discovered that the strongest radioactive source available to us with our risk assessment, Cs-147, was not strong enough to overcome the noise of our system. Due to this, the stronger Am-241 source, which could only be handled by Dr David Cussans, had to be used. This slowed down the experimental process, limiting the time available for data analysis.

Lastly, many hurdles had to be overcome to reduce the inherent noise of the system. Switching power source and resoldering the circuit were tactics used to improve the signal, however both of which were time consuming and therefore also limited the time available for data analysis.

6 Conclusion

6.1 General Evaluation

A scintillating trigger, comprised of a plastic scintillating tile, WLS fibres and SiPM photodetectors, has been researched, designed and tested to measure alpha particles passing through its active area. An accompanying electronics read-out system was designed for testing and analytical purposes, but is not designed to be incorporated into the beamline at CERN's North Area. The final design, with a calculated particle detection efficiency of 99.63%, is compact in size, with an active area of $9cm$x$9cm$, making it easily maneuverable in and out of the beamline. Each component of the design, as stated by each manufacturer's product specification, is radiation tolerant up to and above the required $100kGy$, and the design as a whole is compatible with a vacuum environment. With the recommendations for the future (chapter 6.2) tested and applied as appropriate, the trigger has the potential to be implemented in CERN's experimental areas, replacing the existing, ageing apparatus.

6.2 Recommendations for Improvement

Below is a list of recommendations for improvement of the prototype deisgn itself and also the testing conditions it could be subjected to:

- Mirrors/aluminium foil: use reflective materials at the scintillating tile-WLS fibre boundary to increase light yield and therefore the overall efficiency of the detector.

- Smaller SiPMs: Using SiPMs with a smaller active area would increase material efficiency and also reduce noise as it is proportional to area.

- Optical glue between WLS fibre and SiPM: use glue to improve connection between components so the least amount of light is lost and to improve transmission by minimising Fresnel reflections.

- Use more SiPMs: boost the signal by having connecting an SiPM at both ends of each WLS fibre meaning there would be a total of 4 in each detector.

- Temperature measurements: repeat the testing in colder environments to further reduce noise to achieve clearer photon spikes on recorded data.

- Polishing: higher quality polishing, possibly by a diamond mill, of the ends of the WLS fibre would significantly improve light transmission to the SiPM as less light would be lost via uneven connections between the components

- Improved replication of beam conditions: using a Strontium-90 source to retrieve a better output signal and to better replicate the secondary beam lines in the North Area of CERN.

- Reduce environment noise: undertaking this experiment in Bristol meant that there was a lot of excess electromagnetic noise from the city, which would have affected our system.

A   Python

A.1   Dark Count Rate

```python
# Define time range within file
t_start = 36.5  # us
t_end = 41
mask = (data[:,0] >= t_start) & (data[:,0] <= t_end)
data = data[mask]

# Calculate mean values for each channel over entire time range
mean_A = np.mean(data[:,1])
mean_B = np.mean(data[:,2])

# Define threshold value
val_above = 0.95
threshold_A = mean_A + val_above # mV
threshold_B = mean_B + val_above

# Define time window
window_size = 0.1  # Window width chosen to be width of noise pulse
window_samples = int(window_size / np.mean(np.diff(data[:,0])))  # Creating windows in data


# Define negative trough threshold, most noise pulses are at least this level below channel average
neg_trough = 0.9 # mV

# Find peaks above threshold value for channel A
peaks_A = np.where(data[:,1] > threshold_A)[0]
peak_vals_A = []
peak_times_A = []
for peak in peaks_A:
    if peak >= window_samples and peak <= len(data)-window_samples:
        window_data = data[peak-window_samples:peak+window_samples+1,1] #Picks out data in given window
        max_peak_index = np.argmax(window_data) #Find highest peak within the window
        highest_peak = window_data[max_peak_index]
        if highest_peak == data[peak,1]:
            window_troughs = np.where(window_data < mean_A - neg_trough)[0] #Check if any negative troughs in time window of peak
            if len(window_troughs) == 0: #If no troughs, record this peak
                peak_diff = highest_peak - mean_A #Relate peak height to average of the channel
                peak_vals_A.append(peak_diff)
                peak_times_A.append(data[peak,0])

# Find peaks above threshold value for channel B
peaks_B = np.where(data[:,2] > threshold_B)[0]
peak_vals_B = []
peak_times_B = []
for peak in peaks_B:
    if peak >= window_samples and peak <= len(data)-window_samples:
        window_data = data[peak-window_samples:peak+window_samples+1,2]
        max_peak_index = np.argmax(window_data)
        highest_peak = window_data[max_peak_index]
        if highest_peak == data[peak,2]:
            window_troughs = np.where(window_data < mean_B - neg_trough)[0]
            if len(window_troughs) == 0:
                peak_diff = highest_peak - mean_B
                peak_vals_B.append(peak_diff)
                peak_times_B.append(data[peak,0])


# Print table of peak values and time for each channel
print("Peak table:")
print("Channel A")
print("Time (s)\tPeak value (mV)")
for i in range(len(peak_vals_A)):
    print(f"{peak_times_A[i]}\t\t{peak_vals_A[i]}")
print("Channel B")
print("Time (s)\tPeak value (mV)")
for i in range(len(peak_vals_B)):
    print(f"{peak_times_B[i]}\t\t{peak_vals_B[i]}")

#Set bin width for plots
bin_width = 0.1

# Create histograms for channel A and B
bins = np.arange(min(peak_vals_A), max(peak_vals_A) + bin_width, bin_width)
plt.hist(peak_vals_A, bins=bins, alpha=bin_width, label='Channel A', color = 'red')

bins = np.arange(min(peak_vals_B), max(peak_vals_B) + bin_width, bin_width)
plt.hist(peak_vals_B, bins=bins, alpha=bin_width, label='Channel B', color = 'blue')

plt.title('Frequency of Different Peak Values')
plt.xlabel('Peak Value (mV)')
plt.ylabel('Frequency')
plt.legend()

plt.show()
```

A.2 Final Histograms

```
1
2    import pandas as pd
3    import matplotlib.pyplot as plt
4    import glob
5    import numpy as np
6
7
8    ## Read all CSV files
9    path = 'data/20230323-0018'
10   all_files = glob.glob(path+ '/*.csv' )
11   # print(len(all_files)) # Checking waveform data file length
12
13   #Initial values used for filtering csv files for pulse peaks
14   max_a_arr = []
15   max_b_arr = []
16   thresh = 2.9     #(mV) Minimum value threshold
17   obs_width = 50  # ns value +/- centre of data to observe
18
19   #Retrieving pulse maxima for each waveform
20   i = 0
21   for file in all_files:
22
23       df = pd.read_csv(file)
24       df = df.drop([0])
25       df = df[int(len(df)/2) - obs_width: int(len(df)/2) + obs_width]
26       max_a = float(max(df['Channel A']))
27       max_b = float(max(df['Channel B']))
28       if max_a > thresh and max_b > thresh:
29           max_a_arr.append(max_a)
30           max_b_arr.append(max_b)
31       i+= 1
32
33   print(f'FILES READ: {len(all_files)}')    # Check waveforms have been read
34
35   ##PLOTTING DATA
36   fig , ax = plt.subplots(2, 1,figsize=(24, 36))
37
38   ## Figure parameters
39   font = 12*2
40   font_title = 20*2
41   fontsmall = 10*2
42
43   density = True      #Histogram density param True/False
44   perc_rotate = 75    #Rotation of percentages
45
46   ##FIGURE TITLES
47   # fig.suptitle('Americium Count Rate ' + path)
48   fig.suptitle('Am-241 Source Count Rate - Normalised', fontsize = font_title, y =0.92)
49   # fig.suptitle('No Source Count Rate - Normalised', fontsize = font_title, y =0.92)
50
51   # Bin spacing parameters for histograms
52   bin_end = 13
53   bin_width = 0.1
54   bins = [0]
55   i=0
56
57   while bins[-1] < bin_end:
58       i += bin_width
59       bins.append(round(i,3))
60
61   # Y-axis tick spacing
62   y_end = 2.5
63   y_width = 0.1
64   y_ticks_list = [0]
65   a=0
66
67   while y_ticks_list[-1] < y_end:
68       a += y_width
69       y_ticks_list.append(round(a,2))
70
71
72   ##CREATING HISTOGRAMS FROM DATA
73   # Channel A
74   values_a, bins_a, bars_a  = ax[0].hist(max_a_arr, bins, color = 'r', density = density)
75   ax[0].set_title('Channel A', fontsize = font*1.5)
76   ax[0].grid()
77
78   ax[0].set_xticks(bins, minor = True)
79   ax[0].set_xticks(bins[::5], minor = False)
80   ax[0].set_yticks(y_ticks_list, minor = True)
81   ax[0].set_yticks(y_ticks_list[::5], minor = False)
82   ax[0].set_xticklabels(labels = bins[::5], rotation=90, fontsize = font)
83   ax[0].set_yticklabels(labels = y_ticks_list[::5], fontsize = font)
```

```
84
85
86    # Channel B
87    values_b, bins_b, bars_b  = ax[1].hist(max_b_arr, bins, color = 'b', density = density)
88    ax[1].set_title('Channel B', fontsize = font*1.5)
89    ax[1].grid()
90
91    ax[1].set_xticks(bins, minor = True)
92    ax[1].set_xticks(bins[::5], minor = False)
93    ax[1].set_yticks(y_ticks_list, minor = True)
94    ax[1].set_yticks(y_ticks_list[::5], minor = False)
95    ax[1].set_xticklabels(labels = bins[::5], rotation=90, fontsize = font)
96    ax[1].set_yticklabels(labels = y_ticks_list[::5], fontsize = font)
97
98
99    ##PERCENTAGES AND ERRORS
100   #Channel A
101   rects = ax[0].patches
102   labels = ["label%d" % i for i in range(len(rects))]
103   percent_list = []
104
105   #Error bars A
106   bin_centres = (bins_a[:-1] + bins_a[1:]) / 2
107   y_error = np.random.rand(values_a.size)*(1/len(max_a_arr))*100
108   y_error_mean = np.std(values_a)/ np.sqrt(len(values_a))
109
110   #Plotting Percentages and Error bars on histogram Channel A
111   local_i = 0
112   for rect, label in zip(rects, labels):
113       height = rect.get_height()
114       if height == 0:
115           continue
116       else:
117           index = bins.index(round(rect.get_x(),2))
118           ax[0].text(rect.get_x() + rect.get_width() / 2, height+0.04, s = str(round(height*10,1)) + "%",
119                   ha='center', va='bottom', fontsize = fontsmall, rotation = perc_rotate)
120           percent_list.append(round(height*10,1))
121
122           ax[0].errorbar(x=bin_centres[index], y=values_a[index], yerr=y_error_mean, fmt='.', capsize=4, c = 'green')
123           i += 1
124           # print(bins.index(round(rect.get_x(),2))) #UnComment to observe which bins have data
125
126
127   #Channel B
128   rects = ax[1].patches
129   labels = ["label%d" % i for i in range(len(rects))]
130   percent_list = []
131
132   #Error bars B
133   bin_centres = (bins_b[:-1] + bins_b[1:]) / 2
134   y_error = np.random.rand(values_b.size)*(1/len(max_b_arr))*100
135   y_error_mean = np.std(values_b)/ np.sqrt(len(values_b))
136
137   #Plotting Percentages and Error bars on histogram Channel B
138   local_i = 0
139   for rect, label in zip(rects, labels):
140       height = rect.get_height()
141       if height == 0:
142           continue
143       else:
144           index = bins.index(round(rect.get_x(),2))
145           ax[1].text(rect.get_x() + rect.get_width() / 2, height+0.04, s = str(round(height*10,1)) + "%",
146                   ha='center', va='bottom', fontsize = fontsmall, rotation = perc_rotate)
147           percent_list.append(round(height*10,1))
148
149           ax[1].errorbar(x=bin_centres[index], y=values_b[index], yerr=y_error_mean, fmt='.', capsize=4, c = 'green')
150           i += 1
151
152   #Global Figure Params
153   plt.setp(ax, yticks = y_ticks_list)
154   fig.supxlabel(t = 'Voltage (mV)', fontsize = font*1.5, y=0.07)
155   fig.supylabel(t = 'Normalised Counts', fontsize = font*1.5, x = 0.05)
156   plt.show()
157
```

B SiPM Specification

The model of SiPM used was the Hamamatsu S12572-050P which were given to us by David Cussans in the electronics department of the university. The electrical and optical characteristics are shown in the figure [24] below:

Parameter		Symbol	S12572						Unit
			-025C	-050C	-100C	-025P	-050P	-100P	
Spectral response range		λ	320 to 900			320 to 900			nm
Peak sensitivity wavelength		λp	450			450			nm
Photon detection efficiency (λ=λp)*4		PDE	35			35			%
Dark count*5	Typ.	-	1000			1000			kcps
	Max.		2000			2000			
Time resolution (FWHM)*6		-	250	250	300	250	250	300	ps
Terminal capacitance		Ct	320			320			pF
Gain		M	5.15×10^5	1.25×10^6	2.8×10^6	5.15×10^5	1.25×10^6	2.8×10^6	-
Gain temperature coefficient		ΔTM	8.2×10^3	2.7×10^4	1.2×10^5	8.2×10^3	2.7×10^4	1.2×10^5	/°C
Breakdown voltage		VBR	65 ± 10			65 ± 10			V
Recommended operating voltage		Vop	VBR + 3.5	VBR + 2.6	VBR + 1.4	VBR + 3.5	VBR + 2.6	VBR + 1.4	V
Temperature coefficient of recommended operating voltage		ΔTVop	60			60			mV/°C

Figure 38: A table showing the characteristics for the S12572 series, the SiPM that was used in this application, is in the 5th column headed -050P.

Model S12572-050P allowed us the best time resolution of 250ps whilst maintaining a high gain of 1.25 ± 10^6. The difference between that and the -050C variation is that the -050p variation was a surface mount type package instead of ceramic, meaning it could easily be added to circuit board. It had an active area of 3x3mm; this was bigger than required as the WLS fibre only had a diameter of about 1.25mm and may have contributed to more dark counts than otherwise, but this problem should have been negated by using two and looking for simultaneous hits.

C Material Budget

The material budget used to produce this prototype device was found to be well below the limit set as 5000 CHF. The values given for components and materials in the budget were sourced from local suppliers in the UK and estimates given by manufacturers for invoices of scintillating sheets of EJ-212 and WLS fibre of Kuraray Y-11. This is shown below in Table 1.

Component	Specification	Quantity	Dimensions	Unit Price (GBP)	Total Unit Price	Source
Black 3D printing Filament	n/a	1	0.196 kg	3.71	3.71	Amazon.co.uk
Veroboard	n/a	2	5cm x 2cm	4.4	8.8	RS UK
BNC connectors	50 Ω	2	n/a	2	4	5464853 Coaxial Connectors @ RS UK
Resistors	50 Ω	2	n/a	6.19	12.38	CH0402-50RGF @ Farnell UK
Additional Resistors	100 kΩ	1	n/a	6.96	6.96	RS PRO @ RS UK
Capacitors	100 nF 100V	2	n/a	0.41	0.82	EPCOS B32529
Wire	1/0.25mm	1	n/a	0.216	0.22	Ali Express
EJ -212 Scintillating Tile	n/a	1	100mm x 100mm x 1mm	47	47	Phoenix Dosimetry Ltd
Y-11 WLS	n/a	2	102mm	0.32742	0.65	ThorLabs
Hamamatsu S12572-050P SiPM	n/a	2	3mm x 3mm	66.52	133.04	Hamamatsu
Total GBP					217.58	
Conversion to CHF					242.43	

Table 1

References

[1] Mann, R. 2010. *An Introduction to Particle Physics and the Standard Model* CRC Press 1st edition. DOI:https://doi.org/10.1201/9781420083002

[2] https://www.energy.gov/science/doe-explainsthe-standard-model-particle-physics

[3] Carrol, S. M. et al. directors. 2007.*Dark Matter Dark Energy : The Dark Side of the Universe.*Teaching Company.

[4] Thomson, J. J., 1897. *Cathode Rays* The London, Edinburgh, and Dublin Philosophical Magazine and Journal of Science.DOI: 10.1080/14786449708621070

[5] Bernardo, G. and Konigsberg, J., 2016 *The Standard Theory of Particle Physics World Scientific*, The Higgs Boson Search and Discovery. DOI: 10.1142/9878

[6] https://theconversation.com/cern-scientists-discover-four-new-particles-heres-why-they-matter-155800

[7] Lechner, A., 2018 CERN: *Particle interactions with matter.* CERN Yellow Rep. School Proc., 5, p.47.

[8] Ortega, I., Fosse, L., Franchi, J., Frassier, A., Fullerton, J., Kral, J., Lauener, J., Schneider, T., Spanggaard, J. and Tranquille, G., 2018. *A multipurpose scintillating fibre beam monitor for the measurement of secondary beams at CERN.*

[9] Ortega Ruiz, I., 2018 *Accurate profile measurement of the low intensity secondary beams in the CERN experimental areas* Doctoral dissertation, Ecole Polytechnique, Lausanne.

[10] Buchanan, E. *Bristol Student Project: Scintillating Trigger.* Date of presentation: 13/10/2022. Date accessed: 31/10/2022.

[11] https://home.cern/science/accelerators/accelerator-complex

[12] CERN PhotoLab Archives *https://cds.cern.ch/collection/PhotoLab*

[13] Mapelli, A., 2011. *Scintillation Particle Detectors Based on Plastic Optical Fibres and Microfluidics* (Doctoral dissertation, Ecole Polytechnique, Lausanne).

[14] McDougall, J., 2022. *Literature Review for a Particle Detector Trigger to be Used with Protons.* School of Physics, University of Bristol.

[15] McGrath, A., 2022. *Scintillating Trigger for the Secondary Beams at CERN's North Experimental Area* School of Physics, University of Bristol.

[16] Brackhaus, M., 2022. *Review of the Components of an Intensity Beam Monitor* School of Physics. University of Bristol.

[17] Rizzi, M., D'Aloia, M. and Castagnolo, B., 2010. *Semiconductor detectors and principles of radiation-matter interaction.* Journal of Applied Sciences(Faisalabad), 10(23), pp.3141-3155.

[18] Groom, D.E. and Klein, S.R., 2000. *Passage of particles through matter.* The European Physical Journal C-Particles and Fields, 15(1), pp.163-173.

[19] Jivan, H., Mellado, B., Sideras-Haddad, E., Erasmus, R., Liao, S., Madhuku, M., Peters, G. and Solvyanov, O., 2015, May. *Radiation hardness of plastic scintillators for the Tile Calorimeter of the ATLAS detector.* In Journal of Physics: Conference Series (Vol. 623, No. 1, p. 012016). IOP Publishing.

[20] Kienzle, W., Weisz, S., Burgun, G., Matthiae, G. and Vanderhagen, R., 1975. *Scintillator developments at CERN* (No. CERN-NP-Internal-Report-75-12).

[21] Eljen Technology *General Purpose Plastic Scintillators Product Information*

[22] IUPAC, 1997, *Compendium of Chemical Terminology, 2nd Edition*

[23] Kuraray Co. Ltd *Plastic Scintillating Fibres* Information Documentation

[24] Hamamatsu Photonics *MPPC (Multi Pixel Photon Counter)* S12572-025, -050,-100C/P Datasheet

(https://seltokphotonics.com/upload/iblock/118/1186141f87bc6da48efe2c465195e38d.pdf)

[25] McMillan, J.E., 2005. *Improvements to light collection in scintillation detectors intended for fast cosmic ray timing.*

[26] Ortega, I., Bay, A., Haefeli, G., Spanggaard, J. and Tranquille, G., 2016, October. *A scintillating fibre beam profile monitor for the experimental areas of the SPS at CERN.* In Journal of Physics: Conference Series (Vol. 763, No. 1, p. 012012). IOP Publishing.

[27] Lubsandorzhiev, B.K., 2006. *On the history of photomultiplier tube invention.* Nuclear Instruments and Methods in Physics Research Section A: Accelerators, Spectrometers, Detectors and Associated Equipment, 567(1), pp.236-238.

[28] Piemonte, C. and Gola, A., 2019. *Overview on the main parameters and technology of modern silicon photomultipliers.* Nuclear Instruments and Methods in Physics Research Section A: Accelerators, Spectrometers, Detectors and Associated Equipment, 926, pp.2-15.

[29] Foord, R., Jones, R., Oliver, C.J. and Pike, E.R., 1969. *The use of photomultiplier tubes for photon counting.* Applied optics, 8(10), pp.1975-1989.

[30] Farrell, R., Olschner, F., Shah, K. and Squillante, M.R., 1997. *Advances in semiconductor photodetectors for scintillators.* Nuclear Instruments and Methods in Physics Research Section A: Accelerators, Spectrometers, Detectors and Associated Equipment, 387(1-2), pp.194-198.

[31] Jackson, J. D., 1999. *Classical electrodynamics* (3rd ed.). New York: Wiley. pp. 637–638. ISBN 0-471-30932-X.

[32] Dannheim, D., Elsener, K., van der Kraaij, E., Lucaci Timoce, A. and Klempt, W., 2013. *Particle identification with Cherenkov detectors in the 2011 CALICE tungsten analog hadronic calorimeter test beam at the CERN SPS* (No. LCD-Note-2013-006).

[33] Bovet, C., Maleyran, R., Piemontese, L., Placci, A. and Placidi, M., 1982. *The CEDAR counters for particle identification in the SPS secondary beams: a description and an operation manual* (No. CERN–82-13). European Organization for Nuclear Research.

[34] R. Paschotta, 2008, October *Fresnel reflections in the Encyclopedia of Laser Physics and Technology* 1. edition, Wiley-VCH, ISBN 978-3-527-40828-3

[35] R. Paschotta, 2008, October *Dark Current in the Encyclopedia of Laser Physics and Technology* 1. edition, Wiley-VCH, ISBN 978-3-527-40828-3

[36] LUNDS Universitet, 2009 *WWW Table of Radioactive Isotopes.* LBNL Isotopes Project

[37] Office of Research, University of Cincinnatti